Journal of Wind Engineering & Industrial Aerodynamics 250 (2024) 105783

Contents lists available at ScienceDirect

Journal of Wind Engineering & Industrial Aerodynamics

journal homepage: www.elsevier.com/locate/jweia

Structure of drifting snow simulated by Lagrangian particle dispersion model coupled with large-eddy simulation using the lattice Boltzmann method

Tsutomu Watanabe [a,*], Shuhei Ishikawa [b], Masayuki Kawashima [a], Kou Shimoyama [a], Naoyuki Onodera [c], Yuta Hasegawa [c], Atsushi Inagaki [d]

[a] Institute of Low Temperature Science, Hokkaido University, Sapporo, 060-0819, Japan
[b] Graduate School of Environmental Science, Hokkaido University, Sapporo, 060-0810, Japan
[c] Center for Computational Science & e-Systems, Japan Atomic Energy Agency, Kashiwa, 277-0871, Japan
[d] Department of Transdisciplinary Science and Engineering, Tokyo Institute of Technology, Tokyo, 152-8552, Japan

ARTICLE INFO

Keywords:
Saltation layer height
Force balance
Transition probability
Snow streamers
Low-speed streaks
Ejection
Sweep
Coherent turbulent motion
Atmospheric surface layer

ABSTRACT

This paper describes simulations of drifting snow in the atmospheric surface layer. We develop a Lagrangian particle dispersion model coupled with a large-eddy simulation code based on the central-moment lattice Boltzmann method. The model reproduces typical features of drifting snow observed in the field, such as the dependency of the mass transport rate on the flow velocity, the kink in the vertical mass flux profile near the saltation layer height, and the variations in particle size distribution with the flow velocity and height. The saltation layer height determined directly from the net forces acting on the airborne particles is found to increase monotonically with increasing flow velocity, unlike conventional estimates, which tend to saturate as the flow velocity increases. Using the vertical transition probabilities of individual particles, the transition from saltation to suspension is confirmed to occur near the estimated saltation layer height. A composite analysis shows that snow streamers (dense particle clouds elongated in the streamwise direction and meandering laterally in the saltation layers) are closely associated with small-scale low-speed streaks in the near-surface flows. Particularly dense snow streamers are more likely to occur around streaks modulated by high-speed coherent flows of much larger spatial scales.

1. Introduction

Drifting snow is a significant factor in hazard control because it reduces visibility, creates obstructions through snowdrifts, and produces snow cornices that may trigger avalanches. The large-scale redistribution of snow is known to affect the surface water balance in polar regions and hilly terrain. Terrestrial ecosystems and underground frozen soil in high-latitude and/or high-altitude areas, which are highly sensitive to the spatial distribution of vegetation and micro-topography, can also be profoundly affected by the micro-scale environments produced by heterogeneous depositions of snow (see Mott et al., 2018 for a comprehensive review of wind-driven snow cover dynamics).

Drifting snow is essentially a non-stationary two-phase flow, in which airborne particles and turbulence strongly interact. Further complexity is added by the spatio-temporal intermittencies induced by coherent turbulent motion onto the near-surface flow velocities and the surface processes that feed particles into the flow (Doorschot et al., 2004; Aksamit and Pomeroy, 2018a, 2018b). Therefore, besides the pivotal role of observational and experimental studies, the need for numerical modelling cannot be overemphasized as a means of comprehending the nature of drifting snow phenomena that occur in the atmospheric surface layers.

The first attempt at three-dimensional numerical modelling was made by Uematsu et al. (1991). They modelled drifting snow using an Eulerian advection–diffusion equation for the bulk density of drifting snow particles, which were driven by an airflow simulated by the Reynolds-averaged Navier–Stokes (RANS) equations. Their model was applied to the simulation of snowdrifts around obstacles (Sato et al., 1993). Since then, Tominaga and Mochida (1999), Beyers et al. (2004), and many subsequent studies have refined this type of model and

* Corresponding author.
E-mail address: t-wata@lowtem.hokudai.ac.jp (T. Watanabe).

https://doi.org/10.1016/j.jweia.2024.105783
Received 15 November 2023; Received in revised form 23 May 2024; Accepted 23 May 2024
Available online 1 June 2024

developed improved versions (see Tominaga, 2018; Zhou and Zhang, 2023 for comprehensive reviews of numerical studies on snowdrifts around obstacles). Owing to their computational efficiency, Eulerian models are highly suitable for regional-scale studies (Liston and Sturm, 1998; Gauer, 2001; Liston et al., 2007; Tominaga et al., 2011) and for operational purposes (Pomeroy et al., 1993).

A Lagrangian approach, in which the trajectories of individual particles are traced by integrating the equation of motion, provides a more explicit representation of the particles' behaviour in the flow. The study of Shao and Li (1999) was probably the first to use a Lagrangian particle model coupled with a RANS airflow model for simulating drifting snow. Nemoto and Nishimura (2004) took a similar approach in their simulations of two-dimensional snow-particle trajectories in a coupled one-dimensional flow, and this model was later used by Niiya and Nishimura (2017, 2022). Recently, this type of model has been applied to three-dimensional simulations of drifting snow over roofs (Chen et al., 2021; Liu et al., 2022; Zhou et al., 2023). A remarkable feature of the Lagrangian approach is its ability to realistically reproduce the particle–surface interactions. This is because the key surface processes of the aerodynamic entrainment of particles, the rebound of impacting particles, and the splash entrainment of the snow-bed particles can be directly incorporated into the tracing of individual trajectories.

The intermittency induced by turbulent coherent motion, which RANS models are unable to represent, has motivated the development of next-generation models, namely Lagrangian particle models coupled with large-eddy simulation (LES) models of atmospheric surface-layer flow. Pioneering studies were conducted by Dupont et al. (2013) for drifting soil particles and by Groot Zwaaftink et al. (2014) for drifting snow. Recent studies have used LES-coupled Lagrangian snow-particle models to investigate the horizontal structure of drifting snow (Huang and Wang, 2016), the intermittent nature of drifting snow (Okaze et al., 2018), large-scale drifting snowstorms in the atmospheric boundary layer (Wang and Jia, 2018), sublimation of saltating snow particles (Sharma et al., 2018; Wang et al., 2019), heat and water-vapour transfer during drifting snow events (Sigmund et al., 2022), and the dependency of drifting snow on the snow properties (Melo et al., 2022).

Besides solving the Navier–Stokes equations directly, the lattice Boltzmann method (or algorithm) offers another approach to flow simulation (Chen and Doolen, 1998; Aidun and Clausen, 2010; Krüger et al., 2017). This method considers a fluid as an ensemble of microscopic fluid particles moving around and colliding with each other, and describes fluid motion by the spatio-temporal evolution of the velocity distribution function of the fluid particles. The macroscopic fluid density, velocity, and pressure derived from low-order moments of the distribution function satisfy the Navier–Stokes equations. The method, which has been used successfully in applications ranging from isothermal single-phase flows to fully compressible multiphase flows, can be considered an established solver for the Navier–Stokes equations. As noted by Kareem (2020), it is gaining popularity in engineering applications, such as simulating air flow around buildings (Lenz et al., 2019; Han et al., 2020) and ships (Syms, 2008), and aerodynamics of complex structures (Andre et al., 2015; Islam et al., 2017; Buffa et al., 2021). Recently, the lattice Boltzmann method was confirmed to perform well in simulating atmospheric boundary-layer flows (Ahmad et al., 2017; Inagaki et al., 2017; Onodera et al., 2021; Feng et al., 2021) and atmospheric surface-layer flows including plant canopies (Watanabe et al., 2020, 2021). The computational parallelism shared by the lattice Boltzmann algorithm and the Lagrangian particle model makes their combination appropriate for high-performance computations of drifting snow. The algorithm's flexibility in terms of incorporating complex boundaries is advantageous for simulations of drifting snow over obstacles with complex geometries or time-varying micro-topographies (e.g., snowdrifts) produced by erosion and deposition, and thus will be beneficial for future applications for snow engineering. The application of the lattice Boltzmann method to the simulation of drifting snow was initiated by Tanji et al. (2021), who focused on simulating the wind field around various type of fences and the resulting snowdrift formation. For that purpose, their model did not consider particle–surface interactions or the effects of particle drag on the flow, making it unable to reproduce the self-sustaining nature of drifting snow.

In this paper, we first describe a new Lagrangian particle dispersion model that is fully coupled with the lattice Boltzmann method and includes particle–surface interaction processes. The adopted lattice Boltzmann code, which uses the central-moment-based multi-relaxation-time collision scheme (Geier et al., 2006, 2015), is the same as that used by Watanabe et al. (2020, 2021) to simulate canopy turbulence, and achieves performance comparable to a Navier–Stokes model (Watanabe, 2004, 2009). Aerodynamic entrainment, rebounding, and splash entrainment are included as particle-feeding processes on the snow bed, similar to previous drifting-snow models. We examine the model's ability to reproduce the properties of drifting snow, including instantaneous and statistical features, and investigate the dynamics of saltating particles. Finally, we elucidate the relationship between the horizontal structures of drifting snow and turbulence in the vicinity of the surface.

2. Model description

A Cartesian coordinate system is adopted, in which x, y, and z denote the streamwise, lateral, and vertical directions, respectively. Both the vector notation and the component form of a vector, i.e., $\mathbf{x} = (x,y,z)$, are used in this paper.

2.1. Large-eddy simulation of the near-surface flow

The model used for simulating the turbulent flow in the atmospheric surface layer has been described in our previous reports (Watanabe et al., 2020, 2021); a summary is given here. The model is based on the central-moment lattice Boltzmann method in a three-dimensional 27-velocity (D3Q27) lattice system with a uniform lattice spacing Δx. The method predicts the spatio-temporal evolution of the distribution function $f_{ijk}(\mathbf{x},t)$ of the microscopic fluid-particle velocities (ic, jc, kc), where the indices $i,j,k \in \{-1,0,1\}$ represent the directions of discretized velocities and $c = \Delta x/\Delta t$ denotes the lattice velocity unit, with Δt being the timestep. The velocity distribution function is updated at each timestep through a collision–forcing step followed by a streaming step.

The collision–forcing step begins with the central moments of the distribution function being evaluated by

$$\kappa_{pqr}(\mathbf{x},t) = \sum_{i=-1}^{1}\sum_{j=-1}^{1}\sum_{k=-1}^{1}(ic-u)^p(jc-v)^q(kc-w)^r f_{ijk}(\mathbf{x},t), \tag{1}$$

where κ_{pqr} denotes the central moment of the directional order $p,q,r \in \{0,1,2\}$, and u, v, and w are the streamwise, lateral, and vertical components of the macroscopic velocity $\mathbf{u} = (u,v,w)$, respectively. Using the multi-relaxation-time collision scheme and a forcing scheme applied in the central-moment space, the post-collisional central moments κ^*_{pqr} are calculated in terms of the pre-collisional central moments, the macroscopic fluid density ρ, the macroscopic velocity, a net volumetric force $\mathbf{F} = (F_x,F_y,F_z)$, and the collisional relaxation coefficients $\omega_1,\cdots,\omega_{10}$ as

$$\kappa^*_{pqr}(\mathbf{x},t) = \mathrm{func}(\boldsymbol{\kappa},\rho,\mathbf{u},\mathbf{F}\Delta t,\omega_1,\cdots,\omega_{10}). \tag{2}$$

Details of the above relationship are described in Watanabe et al. (2020). The inverse transform of Eq. (1) is then applied to κ^*_{pqr} to calculate the post-collisional distribution function f^*_{ijk}, which is translated to the adjacent grid points in the next streaming step as

$$f_{ijk}(x+ic\Delta t, y+jc\Delta t, z+kc\Delta t, t+\Delta t) = f^*_{ijk}(x,y,z,t). \tag{3}$$

After appropriate boundary conditions have been applied to this new

distribution function, the macroscopic variables at the next timestep are evaluated from the low-order raw moments as

$$\rho = \sum_{i=-1}^{1}\sum_{j=-1}^{1}\sum_{k=-1}^{1} f_{ijk}, \tag{4a}$$

$$\rho u = \sum_{i=-1}^{1}\sum_{j=-1}^{1}\sum_{k=-1}^{1} (ic) f_{ijk} + \frac{F_x \Delta t}{2}, \tag{4b}$$

$$\rho v = \sum_{i=-1}^{1}\sum_{j=-1}^{1}\sum_{k=-1}^{1} (jc) f_{ijk} + \frac{F_y \Delta t}{2}, \tag{4c}$$

$$\rho w = \sum_{i=-1}^{1}\sum_{j=-1}^{1}\sum_{k=-1}^{1} (kc) f_{ijk} + \frac{F_z \Delta t}{2}, \tag{4d}$$

$$p = \frac{\rho}{3}, \tag{4e}$$

where p is the static pressure. To enable simulations of high Reynolds number flows, the subgrid eddy viscosity ν_e is parametrized using the coherent-structure Smagorinsky model of Kobayashi (2005) and incorporated into the collisional relaxation coefficients for the even-order central moments as $1/\omega = 3(\nu + \nu_e) + 1/2$, where ν is the molecular kinematic viscosity (Watanabe et al., 2020).

The net volumetric force $\mathbf{F}$ is given by the sum of the flow-driving force $\mathbf{F}_{drv}$, the surface friction $\mathbf{F}_s$, and the particle drag $\mathbf{F}_p$. The driving force of the flow is given by

$$\mathbf{F}_{drv} = \left(\frac{\rho u_{*f}^2}{z_{top}}\right)\hat{\mathbf{i}}, \tag{5}$$

where u_{*f} is the friction velocity before the onset of drifting (hereafter referred to as the freestream friction velocity), which is specified for each simulation run, $\hat{\mathbf{i}}$ is the streamwise unit vector, and z_{top} is the height of the computational domain. The surface friction is modelled by a modified bulk drag equation that accounts for the momentum sink caused by particles drifting below the lowest grid level as

$$\mathbf{F}_s = -\rho C_{Ds} |\mathbf{u}_{h,b}| \mathbf{u}_{h,b} / \Delta x - \frac{1}{2}\mathbf{F}_{p,b}, \tag{6}$$

where C_{Ds} is the bulk drag coefficient of the snow surface, $\mathbf{u}_h$ is the horizontal component of the flow velocity, and the subscript b represents variables at the lowest grid level. The bulk drag coefficient is evaluated assuming a logarithmic velocity profile with a prescribed roughness length z_{0s}. The particle drag force $\mathbf{F}_p$ is the sum of the drag forces exerted by all particles within each grid cell, as described in the next subsection.

2.2. Lagrangian model of snow particle motion

The drifting snow particles are assumed to be spherical, and their volume and frontal area are calculated from the particle diameter d_p. Drifting snow particles, while initially complex in shape, tend to break into crystal fragments over the course of multiple impacts on the bed (Sato et al., 2008; Comola et al., 2017), and many of which naturally become more or less rounded rather than retain their original shape (although perfect spheres are rarely observed) (Gordon and Taylor, 2009). The sublimation of the particles is not considered.

2.2.1. Equation of motion

The particles, once seeded to the flow, are accelerated by aerodynamic drag and gravity, and so their velocities and positions change with time. The particle velocity $\mathbf{u}_p$ and the particle position $\mathbf{x}_p$ are determined by

$$\frac{d\mathbf{u}_p}{dt} = \frac{3}{4}\frac{c_d}{d_p}\frac{\rho}{\rho_p}|\Delta u|(\mathbf{u} + \mathbf{u}_s - \mathbf{u}_p) - g\hat{\mathbf{k}}, \tag{7a}$$

$$\frac{d\mathbf{x}_p}{dt} = \mathbf{u}_p, \tag{7b}$$

where ρ_p is the particle density, $|\Delta u|$ is the magnitude of the velocity difference between the particle and the flow, $\mathbf{u}_s$ is the subgrid-scale flow velocity experienced by the particle, g is the acceleration due to gravity, and $\hat{\mathbf{k}}$ is the vertical unit vector. The particle's drag coefficient c_d is evaluated by the empirical formula (White, 1974; Okaze et al., 2018)

$$c_d = \frac{24}{Re_p} + \frac{6}{1 + \sqrt{Re_p}} + 0.4, \tag{8}$$

where $Re_p = d_p|\Delta u|/\nu$ is the particle Reynolds number. This expression is valid for the range $0 \le Re_p \le 2 \times 10^5$ (White, 1974). The flow velocity at the particle position is calculated from the simulated velocities at surrounding grid points by interpolating bilinearly in the horizontal directions and logarithmically in the vertical direction. For the particles below the lowest grid level z_b, the flow velocity is given by $\mathbf{u}(z)/\tilde{\mathbf{u}}(z_b) = \ln[(z + z_{0s})/z_{0s}]/\ln[(z_b + z_{0s})/z_{0s}]$, where $\tilde{\mathbf{u}}(z_b)$ is the horizontal bilinear interpolation of the flow velocity at $z = z_b$. The subgrid-scale flow velocity $\mathbf{u}_s$ is estimated based on the Lagrangian stochastic model described by Weil et al. (2004), as detailed in Appendix A. It should be noted that while these treatments (interpolation of the resolved velocities and modelling of the unresolved velocities) attempt to alleviate the problem caused by insufficient near-surface resolution, some of the results presented in subsequent sections may be dependent on these treatments. However, as the Stokes number near the surface is quite large (see Table 1), the effect of the flow uncertainty on the near-surface particle trajectories may not be significant. Comparisons with much higher resolution simulations are needed to confirm this and are left for future research.

The first term on the right-hand side of Eq. (7a) (denoted here as $\boldsymbol{a}_p$) represents the acceleration induced by the aerodynamic force, the reaction of which exerts a drag force on the flow. Hence, $\mathbf{F}_p$ in the flow model described above is given by

$$\mathbf{F}_p = -\sum \rho_p \frac{\pi d_p^3}{6}\boldsymbol{a}_p, \tag{9}$$

where the summation is taken over all particles in each grid cell.

2.2.2. Aerodynamic entrainment

The entrainment rate N_{ae} [m^{-2} s^{-1}], defined as the number of particles picked up by the flow per unit time and unit area, follows the excess shear stress rule (Anderson and Haff, 1991)

$$N_{ae} = \eta\rho(u_*^2 - u_{*t}^2). \tag{10}$$

Table 1
Relevant parameters for each case of simulations. u_{1m} is the simulated mean wind speed at a height of 1 m. The Reynolds numbers for the flow and particles are defined as $Re_\tau = u_{*f}L/\upsilon$ and $Re_{p,max} = u_{1m}\langle d_p\rangle/\upsilon$, respectively, where L (=4 m) is the height of the domain. The bulk Stokes number St and the viscous Stokes number St^+ are defined as $St = \rho_p\langle d_p\rangle^2 u_{1m}/(18\rho\nu L)$ and $St^+ = \rho_p\langle d_p\rangle^2 u_{*f}^2/(18\rho\nu^2)$, respectively.

u_{*f} [m s^{-1}]	u_{1m} [m s^{-1}]	Re_τ	$Re_{p,max}$	St	St^+
0.3	6.3	9.6×10^4	102	0.19	8.9×10^2
0.35	7.2	1.1×10^5	116	0.22	1.2×10^3
0.4	8.0	1.3×10^5	129	0.26	1.6×10^3
0.5	9.3	1.6×10^5	150	0.29	2.5×10^3
0.6	10.5	1.9×10^5	169	0.32	3.6×10^3
0.8	12.7	2.6×10^5	205	0.39	6.3×10^3

Here, the friction velocity is calculated from $u_* = \sqrt{|\mathbf{F}_s|\Delta x/\rho}$, and the threshold friction velocity u_{*t} is estimated by (Bagnold, 1941)

$$u_{*t} = A\sqrt{\frac{\rho_p - \rho}{\rho} g d_p}, \tag{11}$$

with the constant parameter A set to 0.18 (Clifton et al., 2006). The entrainment coefficient η [N^{-1} s^{-1}] is given by (Clifton and Lehning, 2008)

$$\eta = k_{ae}\frac{4}{\pi\langle d_p\rangle^2}\frac{\rho_s}{\rho_p}, \tag{12}$$

where k_{ae} [m^2 N^{-1} s^{-1}] is a constant parameter set to 1, ρ_s is the surface bulk density of snowpack (set to 150 kg m^{-3}), and angle brackets denote the mean value. The size of each entrained particle is randomly chosen from the size distribution of the snow-bed particles, as specified later. Note that ρ_s is included in Eq. (12) to account for the number of particles available on a unit area of the snow-bed surface and should inherently depend on the snow-bed conditions. However, in most cases, the entrained particles make up only a small fraction of drifting particles (see Section 3.2), so the results presented in this paper are not sensitive to this value.

The initial speed v_{ae} and vertical angle α_{ae} of the entrained particle are specified following Clifton and Lehning (2008) in a similar manner to Groot Zwaaftink et al. (2014). The magnitude of the initial velocity of the entrained particles follows a log-normal distribution with $\langle v_{ae}\rangle = 3.3u_*$ and standard deviation $0.5\langle v_{ae}\rangle$. The mean angle $\langle\alpha_{ae}\rangle$ depends on the particle size and is given by

$$\langle\alpha_{ae}\rangle = \frac{\pi}{180}\left\{75 - 55\left[1 - \exp\left(-\frac{d_p}{1.75\times10^{-4}}\right)\right]\right\}, \tag{13}$$

where individual realizations of the angle obey a log-normal distribution with a standard deviation of $0.5\langle\alpha_{ae}\rangle$. The horizontal angle of ejection is assumed to be parallel to the flow. The entrained particles are launched from a height $z = (\Delta t/2)v_{ae}\sin\alpha_{ae}$ at a randomly chosen horizontal position within each grid area.

2.2.3. Rebound

Snow particles that impact the surface may rebound with a probability P_{rbd} defined by (Anderson and Haff, 1991; Groot Zwaaftink et al., 2014)

$$P_{rbd} = 0.9\left[1 - \exp\left(-2.0|\mathbf{u}_{imp}|\right)\right], \tag{14}$$

where $\mathbf{u}_{imp}$ [m s^{-1}] is the impact velocity. The restitution coefficient of the rebound r_{rbd} is assumed to obey a normal distribution with mean 0.55 and standard deviation 0.1, based on the measurements of Araoka and Maeno (1981), Kosugi et al. (1995), and Nishimura and Hunt (2000). The rebound speed is calculated as $r_{rbd}|\mathbf{u}_{imp}|$, and the vertical angle of rebound follows an exponential distribution with a mean value of 45° (Kok and Renno, 2009), while the horizontal angle is parallel to the incident particle.

2.2.4. Splash

The splash entrainment is the most unknown of the particle feeding processes. The number of splashed particles can be estimated relatively reasonably well under the constraints of conservation of kinetic energy and momentum. However, there are only a few examples of systematic measurements of particle splashing speeds and angles on snow surfaces (e.g., Sugiura and Maeno, 2000), even though they should be affected by many factors, such as snow-bed conditions, properties of impacted particles, impact speed, impact angle. Therefore, statistical relationships established for soil and sand particles from many laboratory and numerical studies are substituted here.

The number of particles that are splashed from the snow bed upon a single particle impact N_{spl} is modelled based on conservation of energy and momentum as (Gauer, 2001; Comola and Lehning, 2017)

$$N_{spl} = \min(N_{se}, N_{sm}), \tag{15a}$$

$$N_{se} = \max\left[\frac{(1 - \delta_{rbd}r_{rbd}^2 - \epsilon_f)m_{imp}|\mathbf{u}_{imp}|^2}{\langle m_{spl}\rangle\langle|\mathbf{u}_{spl}|^2\rangle + 2\phi}, 0\right], \tag{15b}$$

$$N_{sm} = \max\left[\frac{\left(1 - \delta_{rbd}r_{rbd} - \mu_f\right)m_{imp}u_{imp}}{\langle m_{spl}\rangle\langle|\mathbf{u}_{spl}|\rangle\langle\cos\alpha_{spl}\rangle\langle\sin\beta_{spl}\rangle}, 0\right], \tag{15c}$$

where N_{se} and N_{sm} are the numbers estimated from energy and momentum conservation, respectively. Here, $\delta_{rbd} = 1$ if rebound occurs and $\delta_{rbd} = 0$ otherwise, ϵ_f (=0.66; Ammi et al., 2009) and μ_f (=0.35; Rice et al., 1995) are the fractions of kinetic energy and momentum dissipated during the impact, respectively, m_{imp} is the mass of the impacted particle, m_{spl}, $\mathbf{u}_{spl}$, α_{spl}, β_{spl} are the mass, velocity, and vertical and horizontal angles of the splashed particle, respectively, and ϕ [J] is the inter-particle cohesion energy, as determined below. The product $\langle\cos\alpha_{spl}\rangle\langle\sin\beta_{spl}\rangle$ is set to be constant at 0.8 (Comola and Lehning, 2017). The initial motion of a splashed particle is defined by the initial speed, which follows an exponential distribution with $\langle|\mathbf{u}_{spl}|\rangle = 0.25|\mathbf{u}_{imp}|^{0.3}$ (Anderson and Haff, 1991), the vertical angle, which obeys an exponential distribution with $\langle\alpha_{spl}\rangle = 50°$ (Kok and Renno, 2009), and the horizontal angle, which is chosen from a normal distribution around the impact direction with a standard deviation of 15° (Xing and He, 2013). The size of the splashed particle is randomly taken from the size distribution of the snow-bed particles.

Fig. 1 shows the relationship between the impact speed and the number of ejected particles (including both rebounded and splashed particles) obtained from Monte Carlo simulations of the particles' impact–rebound and splashing for different values of ϕ. We followed the procedure of Comola and Lehning (2017), except in using the rebound and splash models described above and the particle size distribution defined by Eq. (16). As the results for $\phi = 3\times10^{-9}$ J best fit the wind-tunnel measurements reported by Sugiura and Maeno (2000), this is taken as the standard value. However, considering the uncertainty in ϕ, which varies depending on the snow-bed conditions, non-cohesive (ϕ

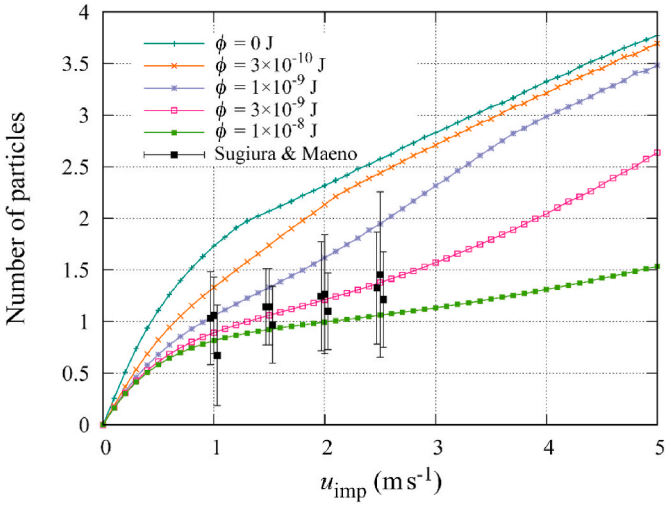

Fig. 1. Mean number of particles ejected (rebounded and splashed) upon a single impact calculated by Monte Carlo simulations using Eqs. (14)–(16) with different cohesive energies. Wind-tunnel measurements reported by Sugiura and Maeno (2000) are also plotted for comparison, with error bars indicating standard deviations. Each simulation performed at 0.1 m s^{-1} intervals in impact speed involves 10^6 particles impacting the surface at randomly sampled angles ranging from 5 to 15°. The sizes of impacting and splashing particles are randomly chosen from the gamma distribution defined by Eq. (16).

$= 0$) and highly cohesive ($\phi = 1 \times 10^{-8}$ J) conditions are also considered in the following simulations. Incidentally, when the same Monte Carlo simulation is performed for single-size non-cohesive particles (e.g., homogeneous sand), the relationship $N_{\mathrm{spl}} \approx 0.5\left|\mathbf{u}_{\mathrm{imp}}\right|$ is observed. This is consistent with previous measurements and numerical simulations (see Fig. 3a of Comola and Lehning, 2017).

2.2.5. Numerical implementation

Aerodynamic entrainment is invoked at a constant time interval Δt_{ae}, with the number of entrained particles calculated from Eq. (10) using the shear stress ρu_*^2 at each surface grid point averaged over Δt_{ae}. By considering the impact–rebound process every timestep, the kinetic energy and momentum remaining after all impact events that occur in each grid area are accumulated over the time interval Δt_{spl}, and these accumulated amounts are used to calculate the number of splashed particles at each Δt_{spl}. Particles entrained (or splashed) at the same time and location are treated as a group of N_{ae} (or N_{spl}) single-sized particles that share the same velocity and position, and each group's trajectory is tracked thereafter. The number of particles belonging to each group (N_{ae} and N_{spl}) retains the fractional part of the number calculated from Eqs. (10) and (15), which is ignored if the number is less than 1. The model code is written in the NVIDIA CUDA language, and the individual trajectories are computed in parallel using graphics processing units.

2.3. Simulation setup

A computational domain of $12.8 \times 12.8 \times 4.0\ \mathrm{m}^3$ with a uniform grid resolution of 0.05 m is used to simulate drifting snow over a flat and homogeneous snow surface under six different wind conditions of $u_{*\mathrm{f}} =$ 0.3, 0.35, 0.4, 0.5, 0.6, and 0.8 m s^{-1}. The top boundary at $z_{\mathrm{top}} = 4$ m is a rigid free-slip wall for the airflow, while the bottom boundary (snow surface) is a rigid wall with friction, as explained in Section 2.1. These rigid-wall boundaries are represented in the lattice Boltzmann algorithm by the half-way specular reflection of the wall-ward components of the velocity distribution function (Watanabe et al., 2020, 2021). The horizontal boundaries are set to be periodic to mimic a developed surface-layer flow over a homogeneous surface. The flow simulations are initialized with a uniform streamwise velocity field with small-magnitude random perturbations of the vertical velocity component. After the turbulence statistics (e.g., mean flow velocity, Reynolds stress, turbulent kinetic energy) reach a steady state, the snow-particle processes are activated to permit the drifting snow to develop over

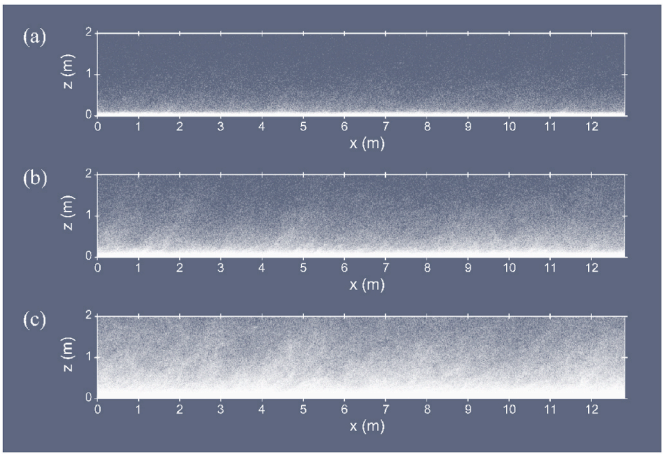

Fig. 2. Vertical–streamwise distribution of particle groups 10 s after the onset of drifting for different values of $u_{*\mathrm{f}}$: (a) 0.35, (b) 0.5, and (c) 0.8 m s^{-1}. All particle groups (see Section 2.2.5) in the lower half of the computational domain are rendered as dots with opacity linearly related to the total cross-sectional area of the particles in each group.

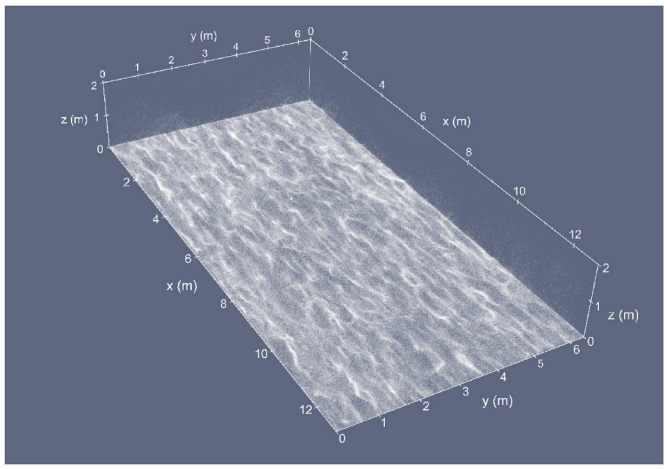

Fig. 3. Horizontal distribution of particle groups obtained at the same instant as for Fig. 2 for the case of $u_{*\mathrm{f}} = 0.5$ m s^{-1}, shown over the half-width of the computational domain.

time. The timestep is the same for the flow and particle motions, and decreases linearly with the freestream friction velocity: from 0.236 ms for $u_{*\mathrm{f}} = 0.3$ m s^{-1} to 8.84×10^{-2} ms for $u_{*\mathrm{f}} = 0.8$ m s^{-1}. The time intervals of aerodynamic entrainment and splash entrainment are set to $\Delta t_{\mathrm{ae}} = \Delta t_{\mathrm{spl}} = 86\Delta t$, which corresponds to 20 ms for the case of $u_{*\mathrm{f}} =$ 0.3 m s^{-1}. With these settings, the number of particle groups tracked ranges from 10^6 to 10^7 depending on $u_{*\mathrm{f}}$, with each group typically containing 10^0 to 10^3 particles. During the simulations, snow particles moving upward beyond the top boundary and stopping (not rebounding) at the surface are discarded.

The density and kinematic viscosity of the air are set to $\rho = 1.34$ kg m^{-3} and $\nu = 1.24 \times 10^{-5}$ m^2 s^{-1}, respectively, and the density of snow particles is set to $\rho_{\mathrm{p}} = 918$ kg m^{-3}. Following Nemoto and Nishimura (2004), the size distribution of the erodible particles on the snow bed is given by a gamma distribution with $\langle d_{\mathrm{p}} \rangle = 2 \times 10^{-4}$ m, expressed as

$$f(d_{\mathrm{p}}) = \frac{d_{\mathrm{p}}^{\alpha-1}}{\beta^{\alpha}\Gamma(\alpha)} \exp\left(-\frac{d_{\mathrm{p}}}{\beta}\right), \tag{16}$$

where $\alpha = 5$ and $\beta = 4 \times 10^{-5}$ m are constant parameters and $\Gamma(\alpha)$ denotes the gamma function. The mean particle mass used in Eq. (15) can be evaluated using $\langle d_{\mathrm{p}}^3 \rangle = \alpha(\alpha+1)(\alpha+2)\beta^3$. Prior to the simulations, a look-up table of cumulative probabilities for 2×10^{-5} m intervals up to the maximum diameter of 6.2×10^{-4} m is prescribed using this formula. The roughness length of the surface is assumed to remain constant at $z_{0\mathrm{s}} = 2.3 \times 10^{-4}$ m (Kondo and Yamazawa, 1986; Gromke et al., 2011). Table 1 summarizes the parameters related to the flow and particles simulated with these settings. Obviously, the flow is fully turbulent, with conditions such that the particles behave as tracers in most of the domain (if the gravity is negligible) and as ballistic projectiles in the region very close to the surface.

Preliminary simulations confirmed that the total mass transport rate reaches steady state by 200 s from the onset of the drifting. Therefore, datasets for post-processing are saved every 1 s for 200–1000 s. Averaging these 800 datasets has also been confirmed sufficient to obtain stable statistics on the fully developed state in which the flow–particle interactions are in equilibrium at all heights in the domain. Unless otherwise stated, the mean values at a given height are calculated as time averages of the horizontal mean values obtained from all datasets, and are denoted by an overbar. Additionally, the particle-related statistics are evaluated at logarithmically equidistant heights, with a finer resolution near the surface than the flow statistics evaluated at each grid level.

3. Results and discussion

3.1. Instantaneous visualization

For a visual inspection of the simulated drifting snow, Figs. 2 and 3 present the vertical and horizontal distributions of the particle groups obtained 10 s after the onset of drifting. Fig. 2 (and its animated version, provided as Supplementary Video 1) illustrates the differences in the height and density of drifting snow (and the resulting visibility reduction) and their growth rates over time at different flow velocities. Fig. 2 also displays the spatial density patterns tilting downstream in the near-surface region, which are affected by coherent eddies developing in the sheared surface-layer flow. The horizontally fluctuating structures commonly seen in the aeolian particle transfer phenomena occurring near the surface (Bass, 2008) are illustrated in Fig. 3 (their temporal variations can be seen in the animation provided as Supplementary Video 2). The spatial relationship between the horizontal patterns in the concentration of drifting particles and the instantaneous flow velocities near the surface will be discussed in Section 3.3.

3.2. Statistics and vertical structure of the drifting snow

3.2.1. Total mass transport rate

The total mass transport rate Q [kg m^{-1} s^{-1}], calculated by integrating the streamwise mass flux with respect to height, is compared with wind-tunnel measurements and empirical formulas derived from such measurements in Fig. 4a. All these wind-tunnel experiments were conducted on smoothly conditioned snow surfaces. Here, for Sørensen's (2004) formula, the parameters proposed by Vionnet et al. (2014) are used and the friction velocity at the impact threshold is assumed to be 0.26 m s^{-1}, which is the equilibrium surface friction velocity obtained from the simulation with $\phi = 0$ for the lowest u_{*f} (=0.3 m s^{-1}).

The simulated values of the transport rate at equilibrium shown in Fig. 4a (filled symbols) are generally smaller than those measured in wind tunnels, especially for small u_{*f} cases; this trend is similar to that reported by Melo et al. (2022). This trend at low u_{*f} may be partly attributable to the intermittency of the aerodynamic entrainment. In the simulations for low-wind-speed conditions, the surface friction velocities do not exceed the threshold simultaneously at all locations because of the higher thresholds for larger particles and the heterogeneity of near-surface turbulent flow. In such a situation, drifting snow occurs only where coherent eddies from aloft enhance the aerodynamic entrainment followed by the splash entrainment of snow-bed particles, as reported by Okaze et al. (2018) and as will be discussed in Section 3.3. This situation contrasts with the wind-tunnel experiments conducted under relatively uniform wind conditions. Meanwhile, even in the non-cohesive case ($\phi = 0$), where the modelled mass transport rate is highest, halving the entrainment threshold (Eq. (11)) or doubling the entrainment coefficient (Eq. (12)) only increases the transport rate by 35% and 20% at $u_{*f} = 0.3$ m s^{-1}, respectively, and does not compensate for the difference from the wind-tunnel results (figure not shown). This is likely due to the negative feedback between wind and particles; as the number of airborne particles increases, wind speed near the surface decreases and the entrainment is reduced.

More importantly, the large sensitivity of Q to ϕ in the low-u_{*f} region indicates the importance of accurate parameterization for the splash entrainment at low wind speeds. As shown in Fig. 1, $\phi = 3 \times 10^{-9}$ J is the value optimized through comparison with direct measurements of the impact–splash process on a snow bed (Sugiura and Maeno, 2000), but the model results using this value nevertheless underestimate the transport rates measured at low wind speeds. The wind-tunnel experiment of Sugiura and Maeno (2000) was conducted at −15 °C to avoid rapid sintering between snow particles, but the actual cohesiveness during the experiment is unknown. Indeed, the model results for $\phi = 0$ are close to Sørensen's formula, but the impact threshold used for this formula is higher than that (0.2 m s^{-1}) measured by Nishimura and Hunt (2000), indicating the model's lower splashing efficiency, even with $\phi = 0$. Incidentally, Anderson and Haff's (1991) numerical experiments for uniform sand grains of 230 μm yielded $N_{spl} \approx 1.5|\mathbf{u}_{imp}|$ (three times larger than the results of our Monte Carlo simulations), and Gauer (2001) used this relationship to parameterize the number of splashed particles. Therefore, we attempted a simulation using three times the N_{spl} value obtained for $\phi = 0$. The resulting mass transport rate during the initial 30 s at $u_{*f} = 0.3$ m s^{-1} is shown by an asterisk in Fig. 4a, and is close to the formula derived by Nishimura and Hunt (2000). However, these results greatly exceed the field observations shown in Fig. 4b. Hence, further study is needed on the model's reproducibility for

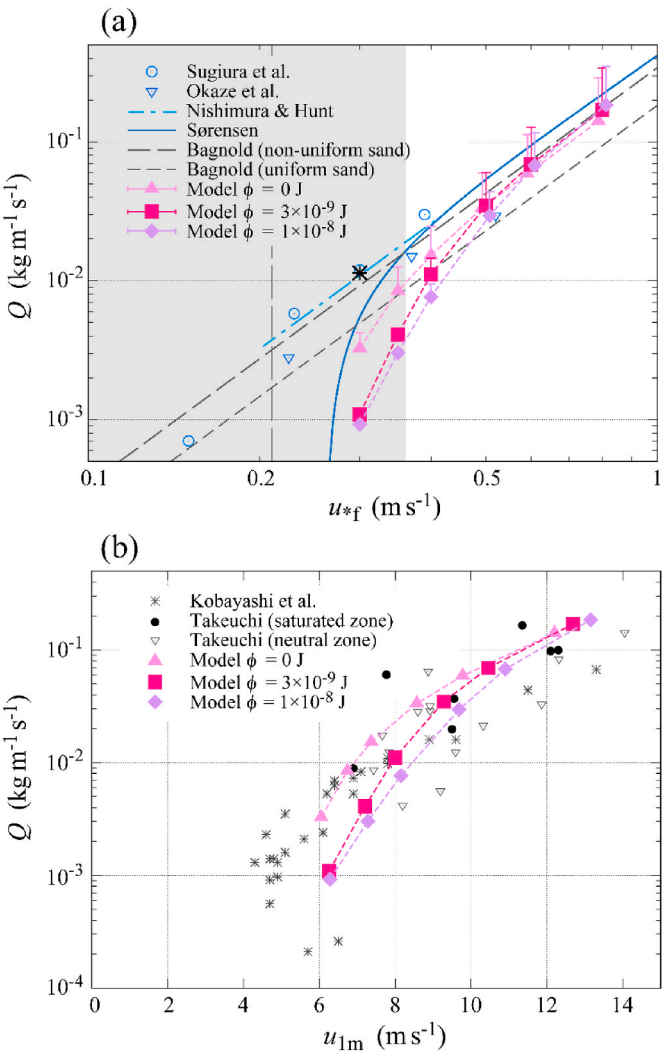

Fig. 4. Total mass transport rates simulated using the different cohesive energies: (a) comparison with wind-tunnel measurements plotted versus the freestream friction velocities; (b) comparison with field observations plotted as a function of the mean wind speed at a height of 1 m. In (a), some model results have been shifted horizontally for clarity; the edges of the error bars indicate the initial transport rates averaged for the first 30 s of each simulation; an asterisk denotes the initial transport rate calculated using three times the N_{spl} value for $\phi = 0$; open circles and open triangles denote wind-tunnel measurements by Sugiura et al. (1998) and Okaze et al. (2012), respectively; the lines represent the empirical formulas of Nishimura and Hunt (2000) and Sørensen (2004) for snow, and Bagnold's (1941) formula for sand; grey shading indicates the range of u_{*t} for the snow-bed particles, and the vertical long-dashed line indicates the u_{*t} corresponding to the mean diameter. In (b), asterisks denote the transport rates observed by Kobayashi et al. (1970) and filled circles and open triangles represent those observed in the saturation zone and in the neutral zone, respectively, by Takeuchi et al. (1975) and Takeuchi (1980).

wind-tunnel experiments at low wind speeds.

The mass transport rate varies significantly with time, especially under high-wind-speed conditions. The transport rate increases rapidly after the onset of drifting and decreases gradually as the near-surface flow slows down because of the particle drag, eventually approaching equilibrium. The model results shown by filled symbols in Fig. 4a are the equilibrium transport rates obtained after the flow and particle statistics reached the steady state throughout the computational domain. There is a significant decrease from the initial transport rates (average of the first 30 s), as indicated by the error bars. These overshoot phenomena have been predicted numerically by Anderson and Haff (1991) and confirmed experimentally by Shao and Raupach (1992), who reported that the minimum distance for saltation to reach equilibrium is approximately 15 m. Even longer fetches (>60 m) were required for the snow transport rate to reach equilibrium in the two-dimensional numerical simulations reported by Zhang and Zhou (2023). Thus, wind-tunnel experiments generally measure the transport rates at some point in the early stages of saltation growth. The model results are therefore in reasonable correspondence with the wind-tunnel measurements, at least for large u_{*f}.

Fig. 4b presents a comparison with field data observed on flat snow surfaces with sufficiently long fetches. The data of Kobayashi et al. (1970) were observed 700 m downwind from the edge of a homogeneous snow surface and were generally obtained under low values of the surface hardness, except for the two smallest values of Q, for which the data were obtained under hard surface conditions. Takeuchi et al. (1975) and Takeuchi (1980) presented data observed in the saturation zone (350 m downwind from the edge), where snowdrift accumulation had just begun to develop in the leeward direction, and data observed in the neutral zone, where neither erosion nor deposition were observed. As shown in the figure, the model results are within the scatter of the observed data. Under low-wind-speed conditions, the results for the non-cohesive case are consistent with Kobayashi's data from the loose surface and tend to approach the hard surface data as the cohesive energy increases. Under high-wind-speed conditions, the three cases of different cohesive energies tend to converge on a single curve, which are most consistent with Takeuchi's data from the saturation zone, where the drifting snow and the air flow are likely to be in equilibrium.

3.2.2. *Vertical profile of horizontal mass flux*

Fig. 5 shows vertical profiles of the mean horizontal mass flux $\overline{q}(z)$. In Fig. 5a, the fluxes simulated using different cohesive energies at $u_{*f} = 0.3$ m s^{-1} are compared with the data observed in Antarctica by Nishimura and Nemoto (2005) under a similar wind condition of $u_{*f} = 0.28$ m s^{-1}. Considering that the conditions of the snowpack at the time of observation are unknown, and that the measurement uncertainty may be large, especially at lower heights where the vertical gradient of the density and velocity of particles is large, the modelled fluxes are in reasonable agreement with the observations, both in magnitude and profile shape. It is notable in Fig. 5a that the reduction in the vertical gradient of flux is reproduced above a height of 0.1–0.2 m, similar to the numerical simulations of Nemoto and Nishimura (2004), Nemoto et al. (2004), and Melo et al. (2022). This kink in the profile reflects the transition from saltation to suspension, with the mass fluxes in the saltation layer being orders of magnitude larger than those aloft in the suspension layer. As confirmed by previous field measurements (e.g., Takeuchi, 1980; Nishimura and Nemoto, 2005; Nishimura et al., 2014), the vertical profile of the horizontal mass flux of saltating snow particles can be approximated by

$$q(z) = q_0 \exp\left(-\frac{z}{L_q}\right), \tag{17}$$

where q_0 is the reference mass flux and L_q is the characteristic decay length. The upper height limit for which Eq. (17) fits to the measured flux has been used as an estimate of the saltation layer height (Sato et al., 2001; Okaze et al., 2012). The fitted results for the fluxes simulated with $\phi = 3 \times 10^{-9}$ J are shown in Fig. 5b, in which the height h_q (determined as the height where the deviation of Eq. (17) exceeds 10% of the flux) is indicated by arrows. The values of q_0, L_q, and h_q obtained from the different u_{*f} cases are listed in Table 2. The height h_q increases with u_{*f} at smaller velocities, but saturates (or even decreases slightly) at larger u_{*f}. The length L_q increases monotonically with u_{*f}, indicating that the vertical gradient of the flux (and hence the difference between the saltation and suspension fluxes) decreases with u_{*f}, consistent with the observations of Nishimura and Nemoto (2005). The saltation flux estimated as $q_0 L_q$ contributes more than 96% of the total mass transport when $u_{*f} = 0.3$ m s^{-1}, but the contribution decreases to 82% in the case of $u_{*f} = 0.8$ m s^{-1}. The relative increase in the contribution of the suspension layer causes an early deviation from the saltation-flux profile (Eq. (17)), which is likely to lead to the saturation of h_q.

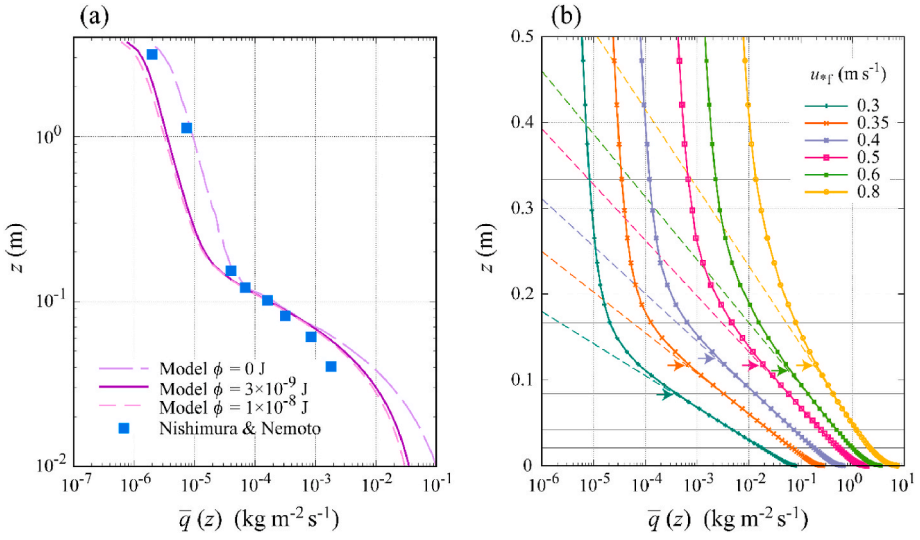

Fig. 5. Vertical profiles of the mean horizontal mass fluxes: (a) fluxes at $u_{*f} = 0.3$ m s^{-1} modelled with different cohesive energies compared with fluxes observed in Antarctica by Nishimura and Nemoto (2005) ($u_{*f} = 0.28$ m s^{-1}); (b) fluxes at different u_{*f} modelled with $\phi = 3 \times 10^{-9}$ J. In (b), dashed lines represent Eq. (17) fitted to the simulated fluxes within the range $0.02 \le z \le 0.5$ m, the arrows indicate the height h_q, determined as the lowest height for which the deviation exceeds 10% of the flux, and horizontal solid lines indicate the selected heights for which the distribution of particle diameters are shown in Fig. 6.

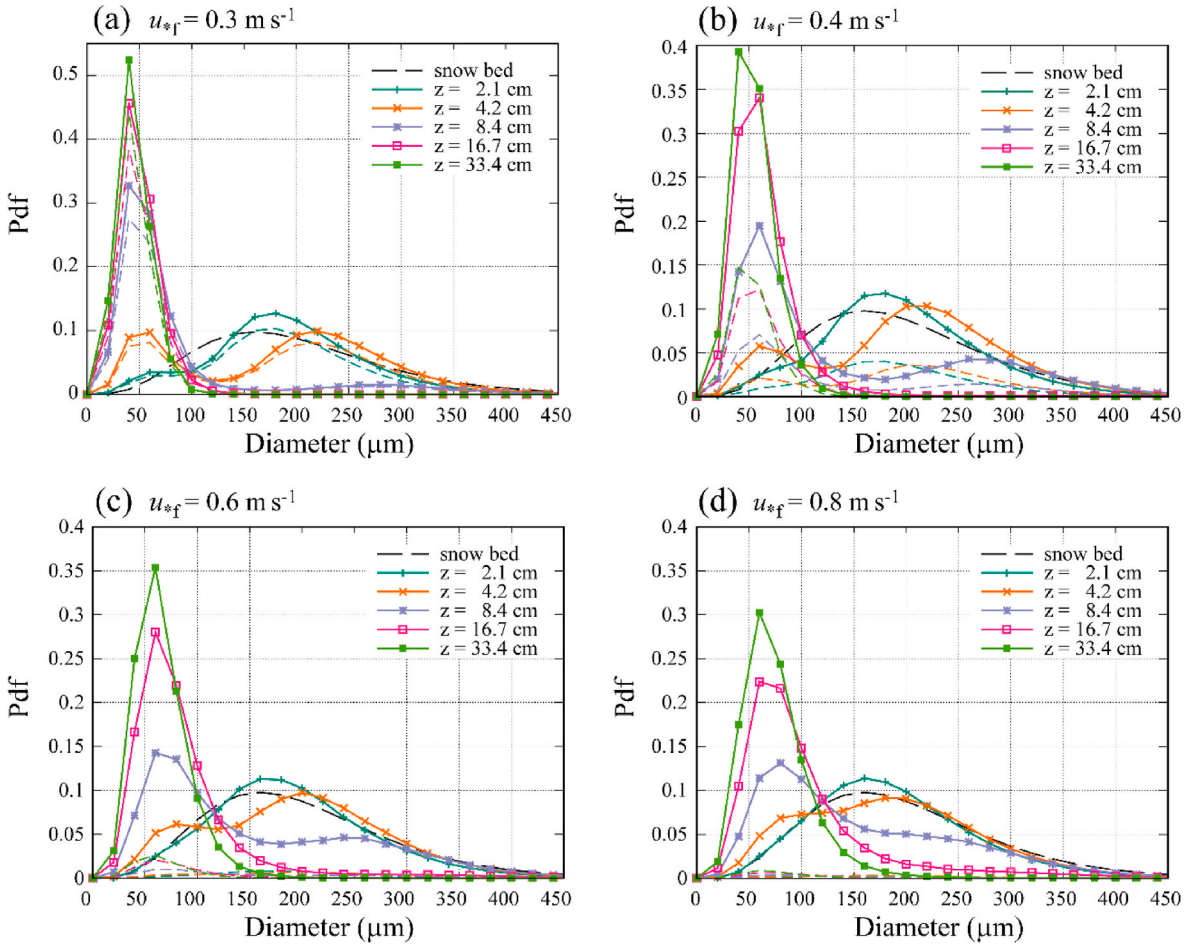

Fig. 6. Probability density function (p.d.f.) of airborne particle diameters for different values of u_{*f}: (a) 0.3, (b) 0.4, (c) 0.6, and (d) 0.8 m s^{-1}. Solid lines represent all particles, including both aerodynamically entrained and splashed particles, while short-dashed lines represent only particles originating from the aerodynamic entrainment. The long-dashed line denotes the p.d.f. prescribed for the snow-bed particle diameters.

Table 2
Parameters relevant to the saltation layer. q_0 and L_q are the parameters of the exponential profile of the mass flux (Eq. (17)), while h_q and h_F are the height of the saltation layer estimated based on the fit of Eq. (17) and the balance of forces acting on individual airborne particles, respectively.

u_{*f} [m s^{-1}]	q_0 [kg m^{-2} s^{-1}]	L_q [cm]	h_q [cm]	h_F [cm]
0.3	6.4×10^{-2}	1.6	8.3	9.1
0.35	0.19	2.1	11.5	10.8
0.4	0.43	2.4	12.5	12.3
0.5	1.1	2.8	11.5	13.9
0.6	1.9	3.2	11.1	14.8
0.8	3.5	4.0	11.7	16.5

3.2.3. Particle size distribution

Fig. 6 shows the probability density function (p.d.f.) of the airborne particle diameters at different heights (indicated in Fig. 5b). In Fig. 6, the solid lines represent all particles, including those both aerodynamically entrained and splashed from the snow bed, while the short-dashed lines represent aerodynamically entrained particles only. Hereafter, the results correspond to simulations using the standard value of $\phi = 3 \times 10^{-9}$ J.

As expected, the particle size distribution is similar to that of the snow bed at lower heights, the distribution shifts to smaller diameters as the height increases, and the distribution at higher positions extends to larger diameters as the wind speed increases. These changes in the p.d.f. with height and wind speed are qualitatively consistent with previous experimental and observational results (Sugiura et al., 1998; Nishimura and Nemoto, 2005). The bimodal shape of the distribution at intermediate heights ($z = 0.042$, 0.088 m), especially prominent at lower wind speeds, reflects the contribution of large particles saltating (with repeated rebounding) on the surface, which is also common to previous simulation results (Nemoto and Nishimura, 2004; Melo et al., 2022). The transition probability profiles shown later (Fig. 8) indicate that particles drifting from various heights remain in a similar height range for a relatively long time. With respect to the particle feeding process, the contribution of splash entrainment is generally dominant, except for the lowest u_{*f} case of these simulations using $\phi = 3 \times 10^{-9}$ J. Additional simulations in which rebounding at the surface is supressed by setting $P_{rbd} = 0$ result in the disappearance of the secondary peaks at large diameters, an increase in the contribution of aerodynamic entrainment, and a significant decrease in the total mass transport rate (figure not shown). These results confirm the importance of a chain reaction in which particles saltating with repeated rebounding over the surface splash off more particles from the snow bed.

3.2.4. Net force acting on drifting particles

In the Lagrangian framework, the acceleration of individual particles at different heights can be assessed directly by examining the net (aerodynamic and gravitational) force acting on the individual particles. The aerodynamic and gravitational forces are evaluated by multiplying the first and second terms on the right-hand side of Eq. (7a) by the particle mass, respectively. Fig. 7 shows the vertical profiles of the net force normalized by the gravitational force acting on each particle,

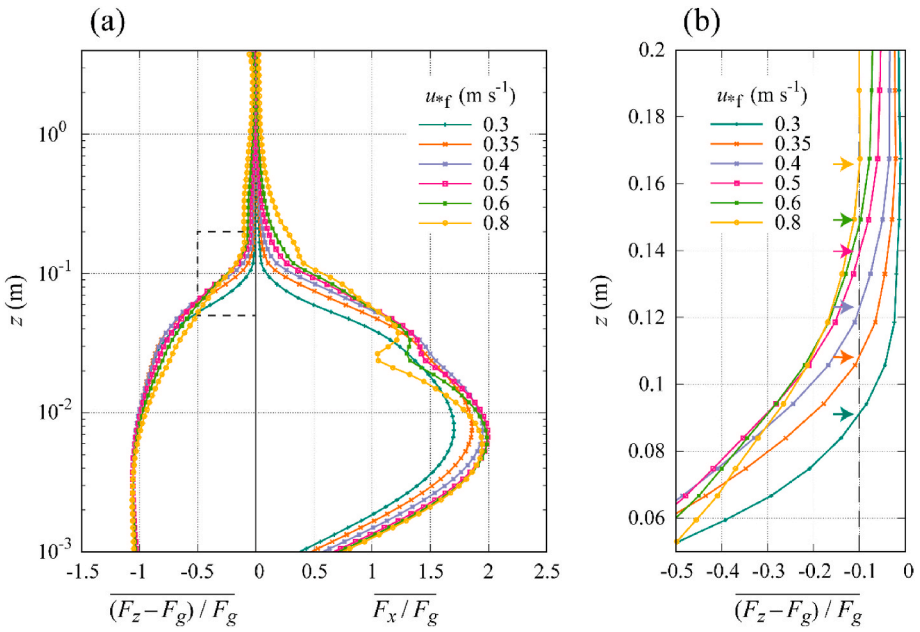

Fig. 7. Vertical profiles of the mean net force normalized by the gravitational force acting on individual particles, averaged over all particles in logarithmically spaced height ranges: (a) profiles over the entire height range; (b) enlarged linear profiles in the dashed rectangular region in (a). F_x and F_z are the streamwise and vertical components of the aerodynamic force, respectively, and F_g is the gravitational force. Data are smoothed using a 1-2-1 vertical filter. Arrows in (b) indicate the height h_F, determined as the lowest height at which the magnitude of the vertical component of the normalized net force decreases below 0.1.

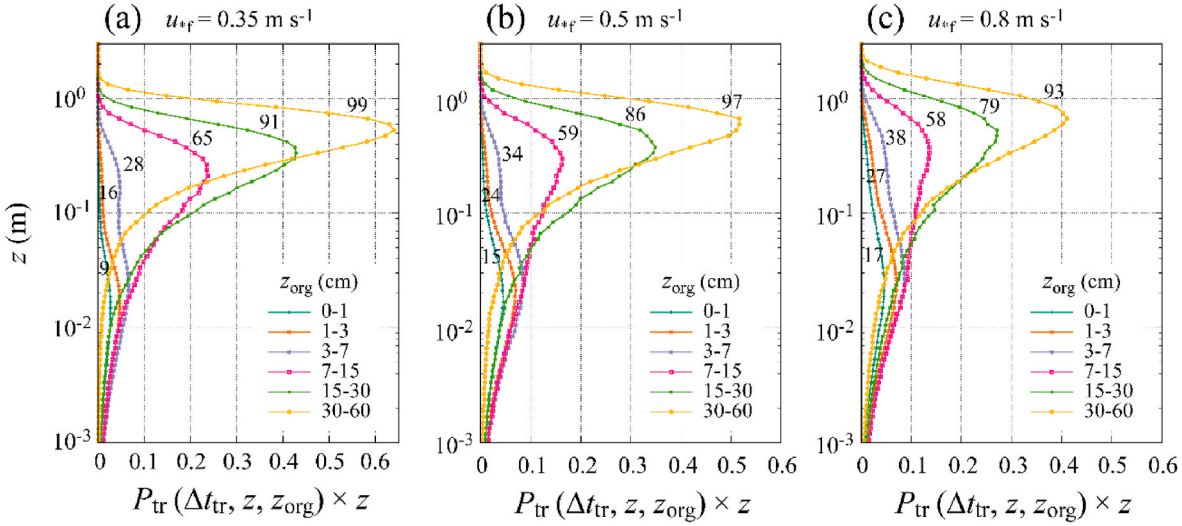

Fig. 8. Profiles of the vertical transition probability of particles originating from different height ranges over the time interval Δt_{tr} = 1 s. Individual panels are for different values of u_{*f}: (a) 0.35, (b) 0.5, and (c) 0.8 m s^{-1}. The numbers associated with each curve denote the total probabilities (%) of particles remaining in the air after 1 s.

averaged over all particles within logarithmically spaced height ranges. The figure indicates that the particles at heights below 0.1–0.2 m are, on average, accelerated in the streamwise direction and decelerated in the vertical direction, thereby producing the streamwise-elongated parabolic trajectories observed in the saltation layer (e.g., Sugiura and Maeno, 2000). At higher levels, the gravitational force is almost counteracted by the vertical component of the aerodynamic force and the streamwise aerodynamic force is generally small (though not zero). This force balance implies that the particles at those heights are almost suspended in the air and follow the flow with only marginal acceleration. Therefore, the lower height limit h_F above which the net force becomes sufficiently small provides another estimate of the saltation layer height. The arrows in Fig. 7b show h_F, estimated as the height at which the magnitude of the normalized net force in the vertical direction decreases below 0.1 (i.e., 90% of gravity is counteracted by the aerodynamic force). The values of h_F are also listed in Table 2. In contrast to h_q, the height h_F increases monotonically with u_{*f}. The streamwise component of the aerodynamic force near h_F increases with wind speed. These facts imply that, under higher wind speeds, larger particles jump high, but are forced to return to the surface while being accelerated in the streamwise direction, forming higher, more elongated parabolic trajectories. Thus, the mean saltation height, estimated purely from the motion of individual particles, increases with wind speed. It should be noted that an arbitrary threshold of 90% is used here because the net force is never completely zero at any altitude as long as the gravity is present. Therefore, the value of h_F should not be taken as an exact value for the

saltation layer height; however, the analysis in the next subsection confirms that h_F gives a reasonable estimate for the transition height from saltation to suspension.

3.2.5. Vertical transition probability of drifting particles

The mean vertical displacement over time of particles at each height can be expressed by the transition probability:

$$P_{\mathrm{tr}}\left(\Delta t_{\mathrm{tr}}, z, z_{\mathrm{org}}\right)=\frac{\sum_{j=1}^{n} N_{\mathrm{ptr}}\left(t_j+\Delta t_{\mathrm{tr}}, z | t_j, z_{\mathrm{org}}\right)}{\sum_{j=1}^{n} N_{\mathrm{p}}\left(t_j, z_{\mathrm{org}}\right)}, \tag{18}$$

where N_{ptr} is the number of particles moving from the original height z_{org} to height z during the time interval Δt_{tr} (=1 s), N_{p} is the total number of particles present at z_{org} at time t_j when the j-th dataset is saved (see Section 2.3), and n is the number of datasets. The vertical profiles of P_{tr} for different ranges of z_{org} are shown in Fig. 8, illustrating the difference in particle fates depending on their original positions. After an interval of 1 s, most particles at levels greater than the estimated height of the saltation layer ($z_{\mathrm{org}} > 0.15$ m) remain suspended in the air, and exhibit a tendency to disperse further upward. As the wind speed increases, the probability distribution of these particles extends not only upward, but also to lower heights, and the total probability decreases. This is because larger particles, which are more abundant in the air under higher wind speeds (Fig. 6), fall faster, as implied by the greater negative vertical force balance shown in Fig. 7. Most particles at heights close to the surface ($z_{\mathrm{org}} < 0.07$ m) settle to the surface within 1 s, while the remaining particles continue saltating at a height of 0.01–0.04 m, producing the minor peak of P_{tr}, with a very small percentage of particles translated to higher levels. This minor peak of P_{tr} disappears in the rebound-inhibited simulations (figure not shown), indicating that it is composed of particles that impacted the surface and rebounded or repeated the process. At intermediate levels near the saltation layer height ($0.07 < z_{\mathrm{org}} < 0.15$ m), approximately 60% of the particles reside in the air after 1 s and tend to displace upward, which represents the transition of particle motion from the saltation mode to the suspension mode (Bagnold, 1941).

3.3. Horizontal structure of the drifting snow

3.3.1. Instantaneous correspondence with the near-surface flow

As often experienced (and as shown in Fig. 3 and the animation provided as Supplementary Video 2), snow drifting over a flat surface forms streamwise-elongated structures, which "merge, bifurcate, and meander laterally back and forth as they move downwind" (Bass, 2008). These are called "snow streamers" or "snow snakes". The spatial relationship between snow streamers and the instantaneous flow field is exemplified in Fig. 9, in which the horizontal positions of large number densities calculated including all particles present within the height range $0.01 < z \leq 0.1$ m in the saltation layer are marked on the horizontal map of instantaneous flow velocities at the lowest grid level ($z = 0.025$ m). The particle number density ρ_{n} [m^{-3}] at a given height follows a roughly log-normal distribution (figure not shown). Thus, the plotting criterion is set as $(\log\rho_{\mathrm{n}})' > \sigma_{\mathrm{LN}}$, where $(\log\rho_{\mathrm{n}})'$ represents a deviation of $\log\rho_{\mathrm{n}}$ from its instantaneous horizontal mean and σ_{LN} is the standard deviation of $\log\rho_{\mathrm{n}}$. Hereafter, a prime ($'$) indicates deviation from the instantaneous horizontal mean. The correspondence between the streamers and the instantaneous flow field is remarkable, with rows containing multiple marks concentrated in the narrow areas of updrafts ($w' > 0$) with slow streamwise velocities ($u' < 0$). Those areas adjacent to or enclosed by a larger-scale longitudinal band of fast streamwise velocities (e.g., $2.5 < y < 5.5$ m) are particularly favourable for the formation of streamers. In contrast, in a slower-velocity band (e.g., $y < 2.5$ m), the marks are sparser, despite a comparable number of updraft regions.

3.3.2. Quadrant analysis

Fig. 10 shows the joint p.d.f. of the turbulent velocity components u' and w', calculated using all datasets for $u_{*\mathrm{f}} = 0.5$ m s^{-1}. In this figure, the grey shading with thin dashed line contours represents the joint p.d.f. of the velocities obtained from all grid points at the lowest level. As expected, in the near-wall boundary layers (Wallace, 2016), u' and w' sampled from the lowest grid points are negatively correlated with each other, constituting the negative Reynolds stress at that level, and their p.d.f. is largely distributed in the quadrants of ejection ($u' < 0$, $w' > 0$) and sweep ($u' > 0$, $w' < 0$). The overlaid bold line contours in Fig. 10a represent a similar p.d.f., but for grid points where the particle number

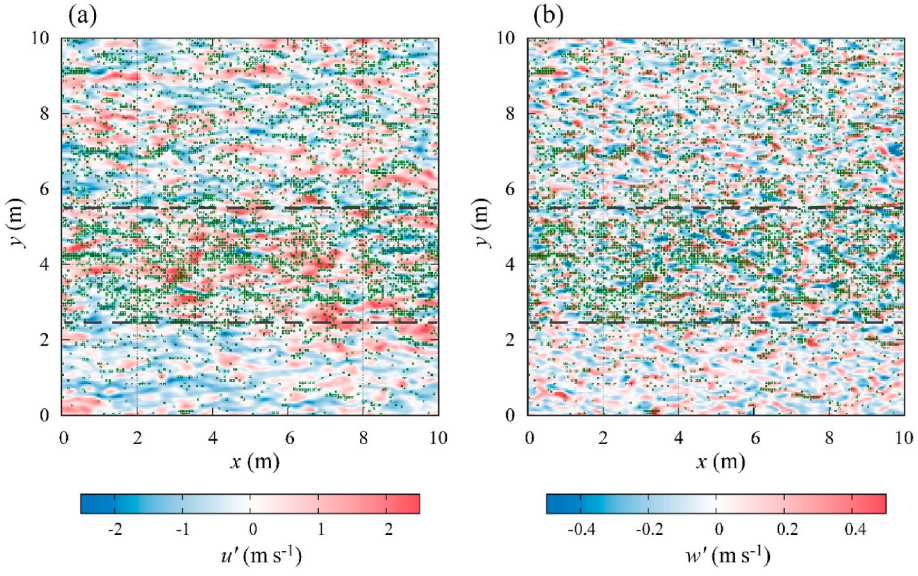

Fig. 9. Instantaneous distribution of dense particle clouds detected in the saltation layer (square dots) plotted over the coloured distribution of the perturbation flow velocities at the lowest grid level: (a) streamwise component and (b) vertical component ($u_{*\mathrm{f}} = 0.5$ m s^{-1}). Dashed lines indicate a large-scale band of fast streamwise velocities.

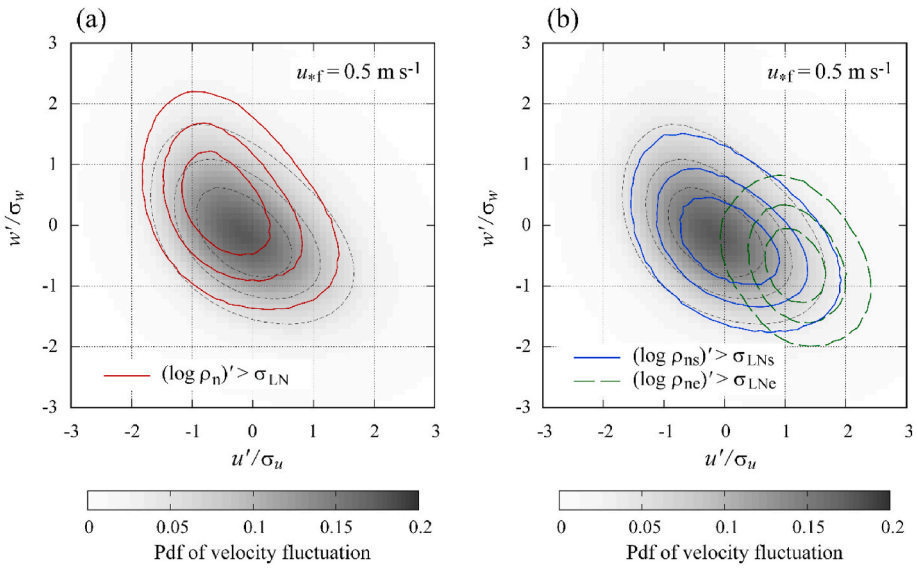

Fig. 10. Joint p.d.f. of the turbulent velocity components u' and w' obtained at the lowest grid level in the case of $u_{*f} = 0.5$ m s^{-1}. σ_u and σ_w are the standard deviations of u' and w', respectively. The grey shading and thin dashed line contours represent the joint p.d.f. of all data at the same level. In (a), the solid line contours denote the joint p.d.f. calculated only from data at grid points where the particle number density within $0.01 < z \leq 0.1$ m satisfies $(\log \rho_n)' > \sigma_{LN}$. In (b), the solid and dashed line contours denote the joint p.d.f. from data at grid points where the number densities within $0 < z \leq 0.01$ m of the freshly splashed particles and freshly entrained particles exceed the threshold, respectively. The line contours are drawn for 25, 50, and 75% of the maxima.

density in the height range $0.01 < z \leq 0.1$ m is sufficient to satisfy $(\log \rho_n)' > \sigma_{LN}$. Compared with the p.d.f. for the entire flow, the joint p.d.f. for velocities at these selected grid points is skewed towards the ejection quadrant, indicating that strong ejection events are involved in the formation of particularly dense particle clouds, which constitute the snow streamers seen in Fig. 9. The skewness towards the ejection is similar to that found by Berk and Coletti (2020) from their wind-tunnel experiments using size-selected glass spheres. To investigate whether there is any correspondence between the development of dense particle clouds and the particle feeding process from the snow bed, a similar analysis is performed for the number densities calculated using only "freshly entrained" and "freshly splashed" particles, i.e., particles that were entrained and splashed at their most recent occurrence (with intervals Δt_{ae} and Δt_{spl}), respectively, and have not yet experienced a rebound. For this analysis, the respective number densities ρ_{ne} and ρ_{ns} are calculated over a height range $0 < z \leq 0.01$ m, which is below the range used to calculate ρ_n. The subscripts e and s denote the freshly entrained and freshly splashed particles, respectively. The results are shown in Fig. 10b, where the bold contours represent the joint p.d.f. of velocities obtained at grid points where $(\log \rho_{ne,s})' > \sigma_{LNe,s}$ is satisfied. The figure clearly shows that aerodynamic entrainment is associated with the most energetic sweep motions. This is because only the strong stresses caused intermittently by these motions exceed the entrainment threshold, ρu_{*t}^2, in the equilibrium state where the surface stresses are (on average) reduced from the freestream value by the drag of airborne particles. Consequently, the contribution of aerodynamic entrainment to the total particle supply is only marginal, as already shown by Fig. 6; this is also evidenced through this analysis by the mean number density of the freshly entrained particles ($\overline{\rho_{ne}} \sim 10^5$ m^{-3}) being two orders of magnitude smaller than that of the freshly splashed particles ($\overline{\rho_{ns}} \sim 10^7$ m^{-3}). Although the p.d.f. of velocities related to the large densities of freshly splashed particles (solid line contours in Fig. 10b) is closer to the background p.d.f. of the entire flow, the distribution is still skewed towards the sweep quadrant, because the faster flow of the sweep motions accelerates the particles impacting the surface more efficiently. The skewness of the p.d.f. for the splash entrainment tends to be smaller for higher u_{*f} cases, but does not show a preference for the ejection quadrant in any scenario (figure not shown). Thus, the dense particle clouds (or streamers), which are associated with ejection motions, are not a direct result of local enhancement of the particle supply at the same locations. Rather, they are formed when airborne particles near the surface, regardless of their origin, gather in narrow regions under the effects of the flow very close to the surface.

3.3.3. *Composite of the flow inducing dense particle clouds near the surface*

The mean spatial structure of the flow causing the dense particle clouds near the surface can be deduced by compositing the conditionally sampled flow variables as

$$\langle \varphi' \rangle (r_x, r_y, z, z_r) = \frac{\sum_{j=1}^{n} \sum_{i=1}^{m_j} \varphi'(x_r^i + r_x, y_r^i + r_y, z)}{\sum_{j=1}^{n} m_j}, \tag{19}$$

where $\langle \varphi' \rangle$ denotes an ensemble average of any flow variable φ' sampled around detection position (x_r^i, y_r^i, z_r) $(i = 1, \cdots, m_j)$, for which the detection condition is satisfied in the j-th dataset, r_x and r_y are the streamwise and lateral displacements from the detection position, respectively, n is the total number of datasets, and m_j is the number of detected points in the j-th dataset. In this analysis, to avoid redundant sampling of the same particle cloud, the detection condition for each dataset is $(\log \rho_n)' > 2\sigma_{LN}$, while ρ_n is calculated over a height range $0.01 < z \leq 0.1$ m, as above.

Fig. 11 shows the horizontal distributions of the composited flow field sliced at $z = 0.025$ m. The figure implies that the dense particle clouds generally occur near the upstream ends of internal ejection regions ($u' < 0$ and $w' > 0$), where near-surface lateral flows converge towards the low-pressure area. The composited low-speed ($u' < 0$) region is elongated in the streamwise direction, measuring about 0.9 m (length) × 0.1 m (width). This is longer than the average streamer length (0.5 m) estimated by Huang and Wang (2016) from numerical simulations in a similar setting to that employed in our study, suggesting that dense particle clouds are generally encompassed within the flow structure that produces them. The streamwise–vertical section at $r_y = 0$ shown in Fig. 12 indicates that the cores of the dense particle clouds tend to be located on the leeward side of tall high-pressure zones (Fig. 12c), which are presumably induced by the stagnation of the streamwise

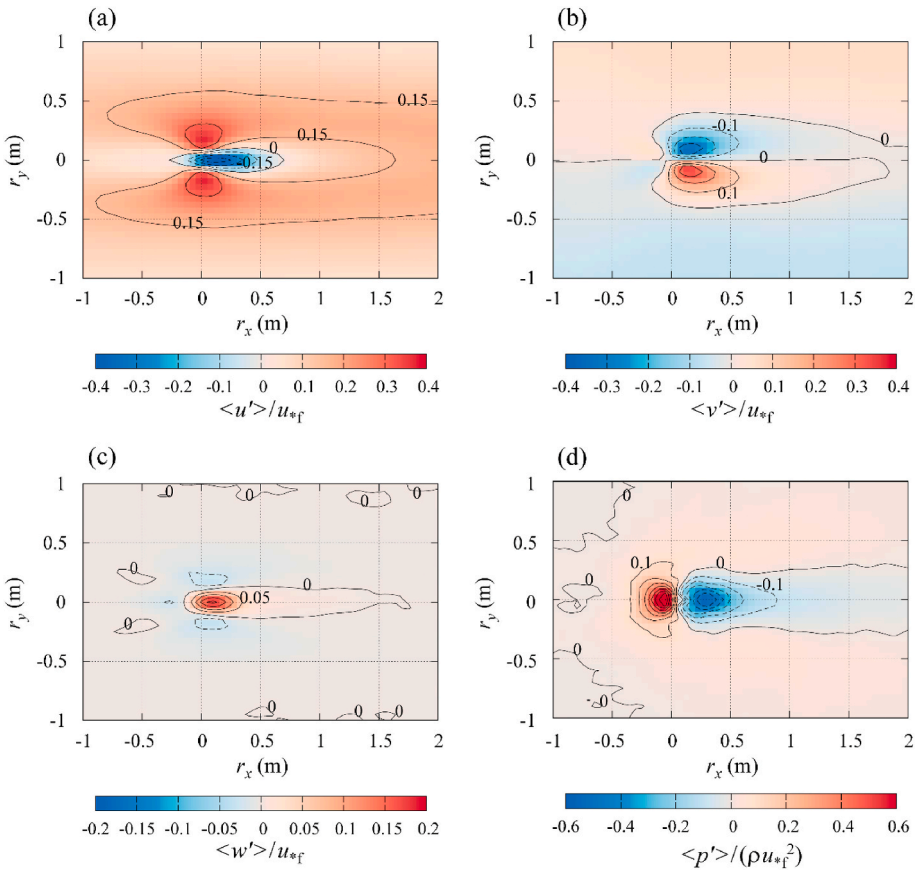

Fig. 11. Horizontal cross-sections at the lowest grid level ($z = 0.025$ m) of the ensemble-averaged flow around the position of particularly dense particle clouds detected at that level: (a) streamwise velocity component $\langle u' \rangle / u_{*f}$, (b) cross-streamwise velocity component $\langle v' \rangle / u_{*f}$, (c) vertical velocity component $\langle w' \rangle / u_{*f}$, and (d) pressure $\langle p' \rangle / \left(\rho u_{*f}^2 \right)$, obtained from the case of $u_{*f} = 0.5$ m s^{-1}. Solid and dashed line contours represent positive and negative values, respectively, and are drawn at intervals of (a) 0.15, (b) 0.1, (c) 0.05, and (d) 0.1.

velocity component near the surface (Fig. 12a). The height of the low-speed region is confined to within 0.2 m, in contrast to the updraft ($w' > 0$) region, which extends higher up and farther downstream (Fig. 12b). These vertical distributions are consistent with the wind-tunnel results of Berk and Coletti (2020), who showed that particles are concentrated in high strain regions of the near-surface turbulent flow. The cross-streamwise–vertical sections sliced at different streamwise positions shown in Fig. 13 indicate that the internal low-speed region is situated between a pair of regions of mean streamwise vorticity with opposite signs. Near the surface, lateral flows from the high-speed regions on both sides converge, inducing the updraft in the middle, and diverge sideways above the vorticity cores. The centre of the vorticity pair lifts slightly downstream. It should be noted, however, that this ensemble-averaged result does not imply the dominance of counter-rotating vortex pairs in the near-surface region. In individual realizations, small-scale single vortices are more commonly identified near the boundary between the inner low-speed region and the surrounding high-speed regions (figure not shown).

With respect to the formation mechanism of snow streamers, Huang and Wang (2016) focused on the suction of small-scale vortices, which may attract saltating snow particles. In contrast, the results of our analysis show that the near-surface velocity patterns produced by the cooperative effects of distributed small-scale vortices, rather than individual vortices themselves, are more closely correlated with the snow streamers. This view does not contradict the finding of Huang and Wang (2016) that snow streamers form in regions flanked on both sides by large-magnitude vorticity (see Fig. 8b in their paper).

3.3.4. *Relationship with large-scale turbulent motion*

The existence of streamwise-elongated low-speed regions near the surface, known as low-speed streaks, is a ubiquitous feature of near-wall boundary-layer flows (Robinson, 1991). The composited flow system described in the previous subsection closely resembles the structure of the near-wall characteristic eddies obtained from direct numerical simulations of channel flow (Moin and Moser, 1989), such as an ejection accompanied by a low-speed streak sandwiched by counter-rotating streamwise vortices that lift downstream, although their spatial scale is much smaller, as the typical streak spacing (known to be 100 viscous wall units) is 1.5–4 mm under the conditions of this study. The present analysis indicates that the near-surface streak structure, which is known to develop through the interaction with small-scale eddies, plays an essential role in the formation of snow streamers, even in high Reynolds number flows in the atmospheric surface layer.

Another remarkable feature is that the composited low-speed streaks are enclosed by large high-speed ($u' > 0$) regions that span most of Figs. 11–13. This reflects the occurrence of streamers being preferentially biased towards the large-scale high-speed bands, as exemplified in Fig. 9. Regarding the particle supply, a larger number of particles are seeded to the flow in the large-scale high-speed regions than in their low-speed counterparts, owing to the enhanced aerodynamic entrainment resulting from larger shear stresses and the increased splashing caused by the acceleration of impacting particles, as indicated by Fig. 10b. The entrained and splashed particles are then gathered by the near-surface convergent flow to form dense particle clouds in the internal low-speed streaks. The activity of near-surface eddies associated with the low-speed streaks is modulated by the coherent turbulent

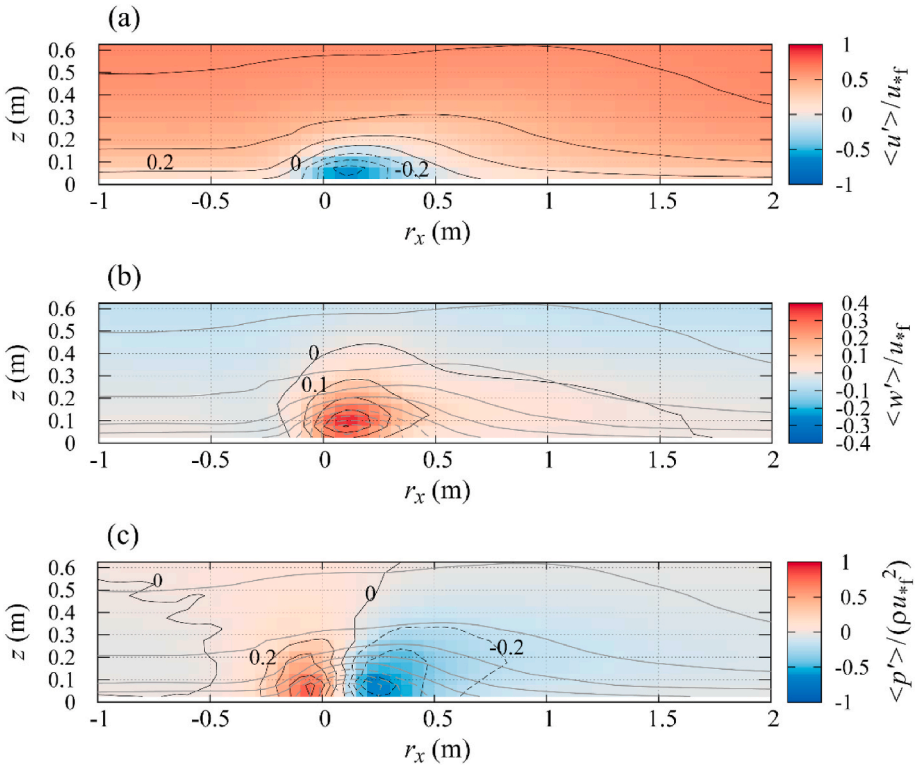

Fig. 12. Streamwise–vertical cross-sections at $r_y = 0$ of the ensemble-averaged flow around the position of particularly dense particle clouds detected at the lowest grid level: (a) streamwise velocity component $\langle u' \rangle / u_{*f}$, (b) vertical velocity component $\langle w' \rangle / u_{*f}$, and (c) pressure $\langle p' \rangle / \left(\rho u_{*f}^2 \right)$, obtained from the case of $u_{*f} = 0.5$ m s^{-1}. Solid and dashed line contours represent positive and negative values, respectively, and are drawn at intervals of (a) 0.2, (b) 0.1, and (c) 0.2. The grey line contours in (b) and (c) replicate the contours of $\langle u' \rangle / u_{*f}$ shown in (a).

motion of much larger spatial scales—the small-scale velocity fluctuations near the surface are amplified within the high-speed regions of the larger coherent motions (Marusic et al., 2010). As demonstrated by Andreolli et al. (2023), the nonlinear energy transfer between large- and small-scale motions, most likely through the stretching of small eddies, is involved in the modulation mechanism. Besides the direct consequence of the more intense internal near-surface flow system, the enhanced activity of small-scale eddies causes the meandering motions of the internal low-speed streaks. Both effects lead to the intensification and fluctuation of the snow streamers formed in the large-scale high-speed regions.

In the atmospheric boundary layers, very large eddies impinging from aloft generate wide high-speed regions (or very large-scale sweeps) near the surface, causing very high spatio-temporal intermittency in the near-surface velocity fluctuations (Hunt and Morrison, 2000). Such eddies are generally scaled with the height of the outer or internal boundary layers and/or regulated by nearby topography. Field observations have shown that the velocity fluctuations associated with such large eddies have a significant impact on the concentration and flux of drifting particles. Aksamit and Pomeroy (2018a,b) observed that the initiation of intensive blowing-snow transport and the increase of the concentration and particle number flux near the surface corresponded to the passage of low-frequency high-speed motions. They also highlighted the role of these high-speed motions that amplify the high-frequency fluctuations in blowing snow density by modulating high-frequency velocity fluctuations. Bass and Sherman (2005) identified that extremely large transport of saltating sand particles occurs in the form of ensembled streamers (similar to that seen in the high-speed band in Fig. 9) during the periods of intermittent high-speed airflow. The latter authors estimated that the spatial scale of sand streamers is determined by the eddies scaled with the height of the internal boundary layer developing over the observation site. Although our simulations do not include the influence of such boundary-layer scale eddies, the results are consistent with these observations in the sense that the large-scale high-speed motions increase the particle supply from the surface and activate the small-scale eddies that contribute to the formation of individual streamers.

4. Conclusions

We have described a Lagrangian particle dispersion model coupled with large-eddy simulation code based on the central-moment lattice Boltzmann method. This model was used to simulate drifting snow in a neutrally stratified turbulent flow within the atmospheric surface layer. The model reproduces typical features of drifting snow observed in the field, such as the dependency of the total mass transport rate on the flow velocity, the kink in the vertical profile of the mass flux near the saltation layer height, and the variations in particle size distribution with flow velocity and height from the snow bed.

The saltation layer height, determined directly from the inspection of forces acting on the airborne particles, increases monotonically with the flow velocity (or the shear stress) above the saltation layer. This is different from conventional estimates, which tend to saturate with increasing flow velocity. The vertical transition probability, which was introduced to evaluate the mean tendency over time of the vertical displacement of individual particles at each height, supports the gradual transition from saltation to suspension around the saltation layer height estimated by the present method.

Regarding the horizontal structure of the saltation layer, snow streamers were found to be closely associated with the appearance of small-scale low-speed streaks formed in the instantaneous flow field near the surface. Particularly dense particle clouds are most often found near the upstream ends of these low-speed streaks, the result of particles being concentrated by near-surface convergent flows. From a larger-

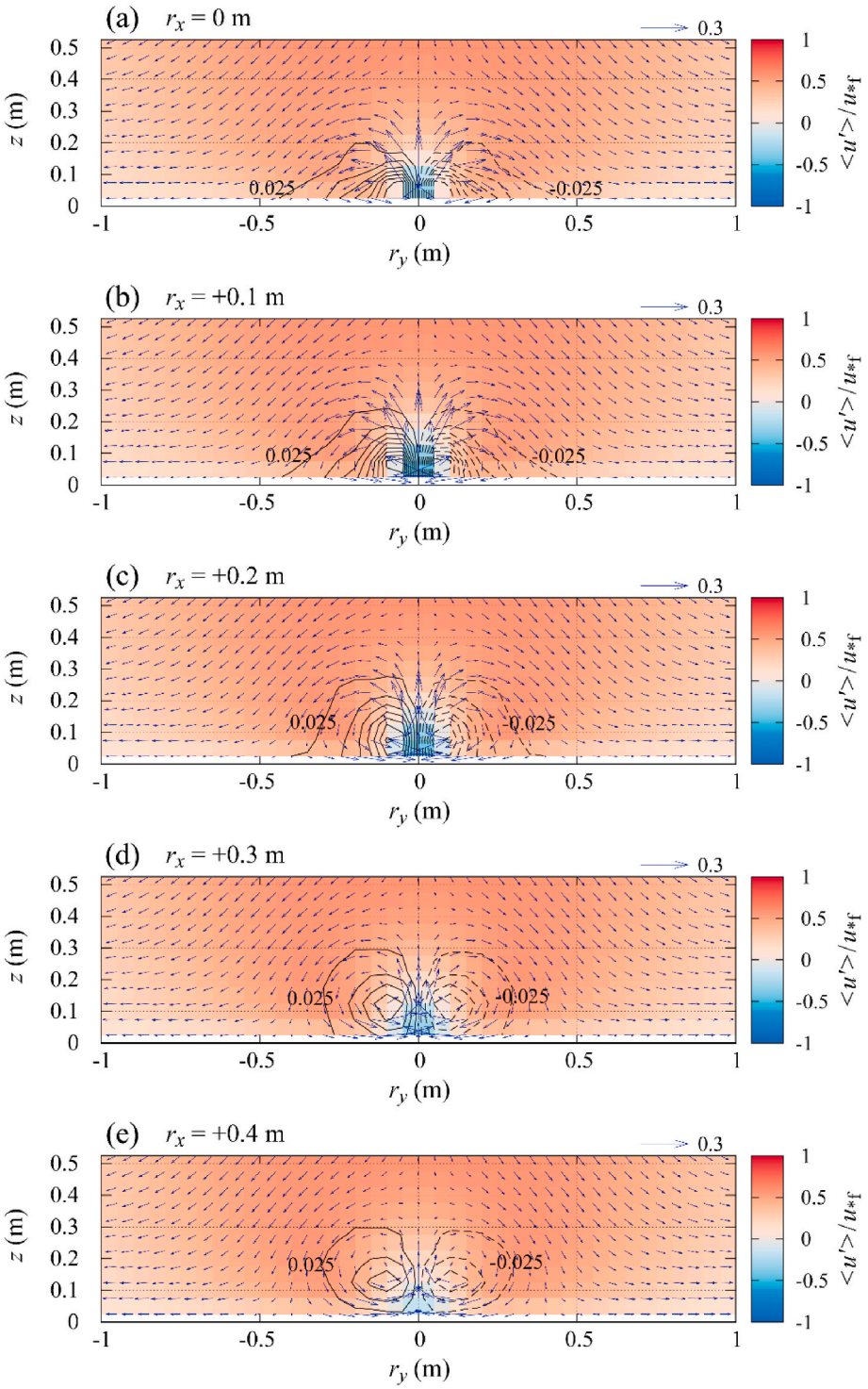

Fig. 13. Cross-streamwise–vertical cross-sections of the ensemble-averaged flow around the position of particularly dense particle clouds detected at the lowest grid level sliced at different r_x: (a) 0 m, (b) +0.1 m, (c) +0.2 m, (d) +0.3 m, and (e) +0.4 m, obtained from the case of $u_{*f} = 0.5$ m s^{-1}. The colour shading indicates $\langle u' \rangle / u_{*f}$, the vectors represent $(\langle v' \rangle / u_{*f}, \langle w' \rangle / u_{*f})$, and the solid and dashed line contours drawn at intervals of 0.05 represent positive and negative values of the streamwise vorticity $\langle \omega_x' \rangle / (u_{*f} / \Delta x)$, respectively.

scale perspective, the low-speed steaks appear almost everywhere near the surface, whereas dense particle clouds are selectively associated with those streaks that are enclosed by high-speed regions of much larger spatial scale. The reasons for this preference are the greater particle supply through the aerodynamic and splash entrainment processes (resulting from the higher flow velocities) and the enhanced activities of small-scale turbulent eddies (most likely owing to increased stretching) in the large-scale high-speed regions. Although the limited computational domain used in this study prevents generalization, we speculate that the preferential occurrence of snow streamers, associated with the large-eddy-modulated low-speed streaks in the vicinity of the snow surface, may be one of the fundamental mechanisms behind the spatio-temporal intermittency of the drifting snow in the surface layers. Further analyses on whether saltating particles affect the near-surface flows and

their modulation in response to the large-scale coherent motions are left for future research.

In terms of model developments, this study only dealt with an ideal situation, i.e. drifting of spherical particles over a flat and homogeneous snow surface under a neutrally stratified atmosphere. Therefore, a reasonable extension of the model enabling its application to more realistic situations would be to include the effects of the buoyancy and sublimation of particles with the aid of appropriate solvers for temperature and humidity in the flow. Consideration of non-spheric particles is also an issue for future research. In such studies, a model of the drag coefficient (e.g., Tagliavini et al., 2021) and general parametrizations of aerodynamic lift forces for particles with complex geometry should be explored. Moreover, using the adaptability of the lattice Boltzmann method to complex boundaries, it is feasible to extend the model to simulate the time-varying surface topographies created by erosion and deposition (around obstacles or on flat surfaces), and the resulting feedback to the turbulent flow. Possible applications of the model framework are not limited to the dispersion of particulate matter such as dust, pollen, sprays, and other aerosols, but also include Lagrangian trajectories of any passive scalar quantities represented as massless particles.

CRediT authorship contribution statement

Tsutomu Watanabe: Writing – original draft, Visualization, Supervision, Software, Resources, Methodology, Funding acquisition, Formal analysis, Conceptualization. **Shuhei Ishikawa:** Writing – review & editing, Visualization, Software, Methodology, Formal analysis. **Masayuki Kawashima:** Writing – review & editing, Methodology. **Kou Shimoyama:** Writing – review & editing, Methodology. **Naoyuki Onodera:** Writing – review & editing, Software, Methodology. **Yuta Hasegawa:** Writing – review & editing, Methodology. **Atsushi Inagaki:** Writing – review & editing, Project administration, Methodology.

Declaration of competing interest

The authors declare that they have no known competing financial interests or personal relationships that could have appeared to influence the work reported in this paper.

Data availability

Data will be made available on request.

Acknowledgements

The authors thank Hirofumi Niiya and Takane Matsumoto (Niigata University) for their fruitful discussions, and Kazuya Ono (Technical Division, Institute of Low Temperature Science, Hokkaido University) for his support with the server maintenance. This work was supported in part by JSPS KAKENHI (Grant Number JP20K04057) and by the Joint Research Program of the Institute of Low Temperature Science, Hokkaido University (Grant Numbers 22G004, 23G008). The authors also thank Edanz (jp.edanz.com) for English language editing.

Appendix A. Subgrid-scale velocity experienced by particles

In the calculation of the particle trajectory, not only resolved fluid velocities but also unresolved, subgrid-scale (SGS) velocities are considered (Eq. (7)). The SGS velocities experienced by the particles are estimated based on the Lagrangian stochastic model proposed by Weil et al. (2004) with some modifications as

$$du_s = \frac{-u_s}{\tau_s}dt + \frac{1}{2}\left(\frac{1}{\sigma_s^2}\frac{d\sigma_s^2}{dt}u_s + \nabla\sigma_s^2\right)dt + \sqrt{\frac{2\sigma_s^2}{\tau_s}}d\xi, \tag{20}$$

where τ_s is the timescale of the SGS velocity, σ_s^2 is the SGS velocity variance evaluated in the large-eddy simulation model, and $d\xi$ is a vector composed of Gaussian white noises $\xi_i \in N(0, dt)$. Following Knorps and Pozorski (2021), τ_s is parametrized as

$$\tau_s = a_\tau \frac{min(\Delta x, z + z_{0s})}{2\sigma_s}, \tag{21}$$

where a_τ, which is a parameter representing the effect of the particle inertia, is assumed constant (=0.5) considering the large Stokes numbers in the near-wall region of our simulations (Table 1). For the particles below the lowest grid level z_b, σ_s is modified as follows:

$$\sigma_s(z) = \sigma_s(z_b)f_1(z) + \sigma_{nw}f_2(z)\ (0 < z < z_b), \tag{22}$$

where σ_{nw} is the near-wall standard deviation of velocities estimated as $\sigma_{nw} = 1.7u$ based on DNS results of channel flow (e.g., Moser et al., 1999) and f_1 and f_2 are logarithmic interpolation functions defined as

$$f_1(z) = \frac{ln(z + z_{0s}) - ln(z_{0s})}{ln(z_b + z_{0s}) - ln(z_{0s})}, \tag{23a}$$

$$f_2(z) = \frac{ln(z_b + z_{0s}) - ln(z + z_{0s})}{ln(z_b + z_{0s}) - ln(z_{0s})}. \tag{23b}$$

For the levels very close to the surface, $z^{+(zu/\nu)<20}$, a linear dumping of $z^+/20$ is applied to the value calculated from Eq. (22).

Appendix B. Supplementary data

Supplementary data to this article can be found online at https://doi.org/10.1016/j.jweia.2024.105783.

References

Ahmad, N.H., Inagaki, A., Kanda, M., Onodera, N., Aoki, T., 2017. Large-eddy simulation of the gust index in an urban area using the lattice Boltzmann method. Boundary-Layer Meteorol. 163, 447–467. https://doi.org/10.1007/s10546-017-0233-6.

Aidun, C.K., Clausen, J.R., 2010. Lattice-Boltzmann method for complex flows. Annu. Rev. Fluid Mech. 42, 439–472. https://doi.org/10.1146/annurev-fluid-121108-145519.

Aksamit, N.O., Pomeroy, J.W., 2018a. The effect of coherent structures in the atmospheric surface layer on blowing-snow transport. Boundary-Layer Meteorol. 167, 211–233. https://doi.org/10.1007/s10546-017-0318-2.

Aksamit, N.O., Pomeroy, J.W., 2018b. Scale interactions in turbulence for mountain blowing snow. J. Hydrometeorol. 19, 305–320. https://doi.org/10.1175/JHM-D-17-0179.1.

Ammi, M., Oger, L., Beladjine, D., Valance, A., 2009. Three-dimensional analysis of the collision process of a bead on a granular packing. Phys. Rev. E 79, 021305. https://doi.org/10.1103/PhysRevE.79.021305.

Anderson, R.S., Haff, P.K., 1991. Wind modification and bed response during saltation of sand in air. In: Barndorff-Nielsen, O.E., Willetts, B.B. (Eds.), Aeolian Grain Transport 1. Acta Mech. Supp. 1. Springer, Vienna, pp. 21–51. https://doi.org/10.1007/978-3-7091-6706-9_2.

Andre, M., Mier-Torrecilla, M., Wüchner, R., 2015. Numerical simulation of wind loads on a parabolic trough solar collector using lattice Boltzmann and finite element methods. J. Wind Eng. Ind. Aerod. 146, 185–194. https://doi.org/10.1016/j.jweia.2015.08.010.

Andreolli, A., Gatti, D., Vinuesa, R., Örlü, R., Schlatter, P., 2023. Separating large-scale superposition and modulation in turbulent channels. J. Fluid Mech. 958, A37. https://doi.org/10.1017/jfm.2023.103.

Araoka, K., Maeno, N., 1981. Dynamical behaviors of snow particles in the saltation layer. Mem. Natl. Inst. Polar Res. - Special Issue 19, 253–263. http://id.nii.ac.jp/1291/00001187.

Bagnold, R.A., 1941. The Physics of Blown Sand and Desert Dunes. Methuen, London.

Bass, A.C.W., 2008. Challenges in aeolian geomorphology: investigating aeolian streamers. Geomorphology 93, 3–16. https://doi.org/10.1016/j.geomorph.2006.12.015.

Bass, A.C.W., Sherman, D.J., 2005. Formation and behavior of aeolian streamers. J. Geophys. Res. 110, F03011 https://doi.org/10.1029/2004JF000270.

Berk, T., Coletti, F., 2020. Transport of inertial particles in high-Reynolds-number turbulent boundary layers. J. Fluid Mech. 903, A18 https://doi.org/10.1017/jfm.2020.597.

Beyers, J.H.M., Sundsbø, P.A., Harms, T.M., 2004. Numerical simulation of three-dimensional, transient snow drifting around a cube. J. Wind Eng. Ind. Aerod. 92, 725–747. https://doi.org/10.1016/j.jweia.2004.03.011.

Buffa, E., Jacob, J., Sagaut, P., 2021. Lattice-Boltzmann-based large-eddy simulation of high-rise building aerodynamics with inlet turbulence reconstruction. J. Wind Eng. Ind. Aerod. 212, 104560 https://doi.org/10.1016/j.jweia.2021.104560.

Chen, S., Doolen, G.D., 1998. Lattice Boltzmann method for fluid flows. Annu. Rev. Fluid Mech. 30, 329–364. https://doi.org/10.1146/annurev.fluid.30.1.329.

Chen, X., Yu, Z., Liu, Z., Cao, R., Zhu, F., 2021. A prediction model for roof snow distribution during long-period snowfall using Eular-Lagrangian method. Cold Reg. Sci. Technol. 190, 103347 https://doi.org/10.1016/j.coldregions.2021.103347.

Clifton, A., Lehning, M., 2008. Improvement and validation of a snow saltation model using wind tunnel measurements. Earth Surf. Process. Landforms 33, 2156–2173. https://doi.org/10.1002/esp.1673.

Clifton, A., Rüedi, J.D., Lehning, M., 2006. Snow saltation threshold measurements in a drifting-snow wind tunnel. J. Glaciol. 52, 585–596. https://doi.org/10.3189/172756506781828430.

Comola, F., Kok, J.F., Gaume, J., Paterna, E., Lehning, M., 2017. Fragmentation of wind-blown snow crystals. Geophys. Res. Lett. 44, 4195–4203. https://doi.org/10.1002/2017GL073039.

Comola, F., Lehning, M., 2017. Energy- and momentum-conserving model of splash entrainment in sand and snow saltation. Geophys. Res. Lett. 44, 1601–1609. https://doi.org/10.1002/2016GL071822.

Doorschot, J.J.J., Lehning, M., Vrouwe, A., 2004. Field measurements of snow-drift threshold and mass fluxes, and related model simulations. Boundary-Layer Meteorol. 113, 347–368. https://doi.org/10.1007/s10546-004-8659-z.

Dupont, S., Bergametti, G., Marticorena, B., Simoëns, S., 2013. Modeling saltation intermittency. J. Gehophys. Res. Atmos. 118, 7109–7128. https://doi.org/10.1002/jgrd.50528.

Feng, Y., Miranda-Fuentes, J., Guo, S., Jacob, J., Sagaut, P., 2021. ProLB: a lattice Boltzmann solver of large-eddy simulation for atmospheric boundary layer flows. J. Adv. Model. Earth Syst. 13, e2020MS002107 https://doi.org/10.1029/2020MS002107.

Gauer, P., 2001. Numerical modeling of blowing and drifting snow in Alpine terrain. J. Glaciol. 47, 97–110. https://doi.org/10.3189/172756501781832476.

Geier, M., Greiner, A., Korvink, J.G., 2006. Cascaded digital lattice Boltzmann automata for high Reynolds number flow. Phys. Rev. E 73, 066705. https://doi.org/10.1103/PhysRevE.73.066705.

Geier, M., Schönherr, M., Pasquali, A., Krafczyk, M., 2015. The cumulant lattice Boltzmann equation in three dimensions: theory and validation. Comput. Math. Appl. 70, 507–547. https://doi.org/10.1016/j.camwa.2015.05.001.

Gordon, M., Taylor, P.A., 2009. Measurements of blowing snow, Part I: particle shape, size distribution, velocity, and number flux at Churchill, Manitoba, Canada. Cold Reg. Sci. Technol. 55, 63–74. https://doi.org/10.1016/j.coldregions.2008.05.001.

Gromke, C., Manes, C., Walter, B., Lehning, M., Guala, M., 2011. Aerodynamic roughness length of fresh snow. Boundary-Layer Meteorol. 141, 21–34. https://doi.org/10.1007/s10546-011-9623-3.

Groot Zwaaftink, C.D., Diebold, M., Horender, S., Overney, J., Lieberherr, G., Parlange, M.B., Lehning, M., 2014. Modelling small-scale drifting snow with a Lagrangian stochastic model based on large-eddy simulations. Boundary-Layer Meteorol. 153, 117–139. https://doi.org/10.1007/s10546-014-9934-2.

Han, M., Ooka, R., Kikumoto, H., 2020. Validation of lattice Boltzmann method-based large-eddy simulation applied to wind flow around single 1:1:2 building model. J. Wind Eng. Ind. Aerod. 206, 104277 https://doi.org/10.1016/j.jweia.2020.104277.

Huang, N., Wang, Z.S., 2016. The formation of snow streamers in the turbulent atmosphere boundary layer. Aeolian Res 23, 1–10. https://doi.org/10.1016/j.aeolia.2016.09.002.

Hunt, J.C.R., Morrison, J.F., 2000. Eddy structure in turbulent boundary layers. Eur. J. Mech. B 19, 673–694. https://doi.org/10.1016/S0997-7546(00)00129-1.

Inagaki, A., Kanda, M., Ahmad, N.H., Yagi, A., Onodera, N., Aoki, T., 2017. A numerical study of turbulence statistics and the structure of a spatially-developing boundary layer over a realistic urban geometry. Boundary-Layer Meteorol. 164, 161–181. https://doi.org/10.1007/s10546-017-0249-y.

Islam, A., Gaylard, A., Thornber, B., 2017. A detailed statistical study of unsteady wake dynamics from automotive bluff bodies. J. Wind Eng. Ind. Aerod. 171, 161–177. https://doi.org/10.1016/j.jweia.2017.09.009.

Kareem, A., 2020. Emerging frontiers in wind engineering: computing, stochastics, machine learning and beyond. J. Wind Eng. Ind. Aerod. 206, 104320 https://doi.org/10.1016/j.jweia.2020.104320.

Knorps, M., Pozorski, J., 2021. Stochastic modeling for subgrid-scale particle dispersion in large-eddy simulation of inhomogeneous turbulence. Phys. Fluids 33, 043323. https://doi.org/10.1063/5.0046320.

Kobayashi, D., Kobayashi, S., Ishikawa, N., 1970. Measurement of snow drift using parallel trenches. Low Temp. Sci. 27, 99–106 (in Japanese with English summary). http://hdl.handle.net/2115/18104.

Kobayashi, H., 2005. The subgrid-scale models based on coherent structures for rotating homogeneous turbulence and turbulent channel flow. Phys. Fluids 17, 045104. https://doi.org/10.1063/1.1874212.

Kok, J.F., Renno, N.O., 2009. A comprehensive numerical model of steady state saltation (COMSALT). J. Geophys. Res. 114, D17204 https://doi.org/10.1029/2009JD011702.

Kondo, J., Yamazawa, H., 1986. Bulk transfer coefficient over a snow surface. Boundary-Layer Meteorol. 34, 123–135. https://doi.org/10.1007/BF00120912.

Kosugi, K., Nishimura, K., Maeno, N., 1995. Studies on the dynamics of saltation in drifting snow. Rep. Natl. Res. Inst. Earth Sci. Disaster Prev. 54, 111–154. https://doi.org/10.24732/nied.00001063.

Krüger, T., Kusumaatmaja, H., Kuzmin, A., Shardt, O., Silva, G., Viggen, E.M., 2017. The Lattice Boltzmann Method: Principles and Practice. Springer.

Lenz, S., Schönherr, M., Geier, M., Krafczyk, M., Pasquali, A., Christen, A., Giometto, M., 2019. Towards real-time simulation of turbulent air flow over a resolved urban canopy using the cumulant lattice Boltzmann method on a GPGPU. J. Wind Eng. Ind. Aerod. 189, 151–162. https://doi.org/10.1016/j.jweia.2019.03.012.

Liston, G.E., Sturm, M., 1998. A snow-transport model for complex terrain. J. Glaciol. 44, 498–516. https://doi.org/10.3189/S0022143000002021.

Liston, G.E., Haehnel, R.B., Strum, M., Hiemstra, C.A., Berezovskaya, S., Tabler, R.D., 2007. Simulating complex snow distributions in windy environments using SnowTran-3D. J. Glaciol. 53, 241–256. https://doi.org/10.3189/172756507782202865.

Liu, Z., Zhou, X., Gu, M., 2022. A numerical model for snow drifting simulations on flat roofs using Lagrangian approach. J. Wind Eng. Ind. Aerod. 222, 104922 https://doi.org/10.1016/j.jweia.2022.104922.

Marusic, I., Mathis, R., Hutchins, N., 2010. Predictive model for wall-bounded turbulent flow. Science 329, 193–196. https://doi.org/10.1126/science.1188765.

Melo, D.B., Sharma, V., Comola, F., Sigmund, A., Lehning, M., 2022. Modeling snow saltation: the effect of grain size and interparticle cohesion. J. Geophys. Res. Atmos. 127, e2021JD035260 https://doi.org/10.1029/2021JD035260.

Moin, P., Moser, R.D., 1989. Characteristic-eddy decomposition of turbulence in a channel. J. Fluid Mech. 200, 471–509. https://doi.org/10.1017/S0022112089000741.

Moser, R.D., Kim, J., Mansour, N.N., 1999. Direct numerical simulation of turbulent channel flow up to $Re_\tau = 590$. Phys. Fluids 11, 943–945. https://doi.org/10.1063/1.869966.

Mott, R., Vionnet, V., Grünewald, T., 2018. The seasonal snow cover dynamics: review on wind-driven coupling processes. Front. Earth Sci. 6, 197. https://doi.org/10.3389/feart.2018.00197.

Nemoto, M., Nishimura, K., 2004. Numerical simulation of snow saltation and suspension in a turbulent boundary layer. J. Geophys. Res. 109, D18206 https://doi.org/10.1029/2004JD004657.

Nemoto, M., Nishimura, K., Kobayashi, S., Izumi, K., 2004. Numerical study of the time development of drifting snow and its relation to the spatial development. Ann. Glaciol. 38, 343–350. https://doi.org/10.3189/172756404781815202.

Niiya, H., Nishimura, K., 2017. Spatiotemporal structure of aeolian particle transport on flat surface. J. Phys. Soc. Japan 86, 054402. https://doi.org/10.7566/JPSJ.86.054402.

Niiya, H., Nishimura, K., 2022. Hysteresis and surface shear stresses during snow-particle aeolian transportation. Boundary-Layer Meteorol. 183, 447–467. https://doi.org/10.1007/s10546-022-00688-8.

Nishimura, K., Yokoyama, C., Ito, Y., Nemoto, M., Naaim-Bouvet, F., Bellot, H., Fujita, K., 2014. Snow particle speeds in drifting snow. J. Geophys. Res. Atmos. 119, 9901–9913. https://doi.org/10.1002/2014JD021686.
Nishimura, K., Hunt, J.C.R., 2000. Saltation and incipient suspension above a flat particle bed below a turbulent boundary layer. J. Fluid Mech. 417, 77–102. https://doi.org/10.1017/S0022112000001014.
Nishimura, K., Nemoto, M., 2005. Blowing snow at Mizuho station, Antarctica. Phil. Trans. R. Soc. A 363, 1647–1662. https://doi.org/10.1098/rsta.2005.1599.
Okaze, T., Mochida, A., Tominaga, Y., Nemoto, M., Sato, T., Sasaki, Y., Ichinohe, K., 2012. Wind tunnel investigation of drifting snow development in a boundary layer. J. Wind Eng. Ind. Aerod. 104–106, 532–539. https://doi.org/10.1016/j.jweia.2012.04.002.
Okaze, T., Niiya, H., Nishimura, K., 2018. Development of a large-eddy simulation coupled with Lagrangian snow transport model. J. Wind Eng. Ind. Aerod. 183, 35–43. https://doi.org/10.1016/j.jweia.2018.09.027.
Onodera, N., Idomura, Y., Hasegawa, Y., Nakayama, H., Shimokawabe, T., Aoki, T., 2021. Real-time tracer dispersion simulations in Oklahoma City using the locally mesh-refined lattice Boltzmann method. Boundary-Layer Meteorol. 179, 187–208. https://doi.org/10.1007/s10546-020-00594-x.
Pomeroy, J.W., Gray, D.M., Landine, P.G., 1993. The Prairie blowing snow model: characteristics, validation. operation. J. Hydrol. 144, 165–192. https://doi.org/10.1016/0022-1694(93)90171-5.
Rice, M.A., Willetts, B.B., McEwan, I.K., 1995. An experimental study of multiple grain-size ejecta produced by collisions of saltating grains with a flat bed. Sedimentology 42, 695–706. https://doi.org/10.1111/j.1365-3091.1995.tb00401.x.
Robinson, S.K., 1991. Coherent motions in the turbulent boundary layer. Annu. Rev. Fluid Mech. 23, 601–639. https://doi.org/10.1146/annurev.fl.23.010191.003125.
Sato, T., Kosugi, K., Mochizuki, S., Nemoto, M., 2008. Wind speed dependences of fracture and accumulation of snowflakes on snow surface. Cold Reg. Sci. Technol. 51, 229–239. https://doi.org/10.1016/j.coldregions.2007.05.004.
Sato, T., Kosugi, K., Sato, A., 2001. Saltation-layer structure of drifting snow observed in wind tunnel. Ann. Glaciol. 32, 203–208. https://doi.org/10.3189/172756401781819184.
Shao, Y., Li, A., 1999. Numerical modelling of saltation in the atmospheric surface layer. Boundary-Layer Meteorol. 91, 199–225. https://doi.org/10.1023/A:1001816013475.
Sato, T., Uematsu, T., Nakata, T., Kaneda, Y., 1993. Three dimensional numerical simulation of snowdrift. J. Wind Eng. Ind. Aerod. 46/47, 741–746. https://doi.org/10.1016/B978-0-444-81688-7.50082-6.
Shao, Y., Raupach, M.R., 1992. The overshoot and equilibration of saltation. J. Geophys. Res. 97, 20559–20564. https://doi.org/10.1029/92JD02011.
Sharma, V., Comola, F., Lehning, M., 2018. On the suitability of the Thorpe–Mason model for calculating sublimation of saltating snow. Cryosphere 12, 3499–3509. https://doi.org/10.5194/tc-12-3499-2018.
Sigmund, A., Dujardin, J., Comola, F., Sharma, V., Huwald, H., Melo, D.B., Hirasawa, N., Nishimura, K., Lehning, M., 2022. Evidence of strong flux underestimation by bulk parametrizations during drifting and blowing snow. Boundary-Layer Meteorol. 182, 119–146. https://doi.org/10.1007/s10546-021-00653-x.
Sørensen, M., 2004. On the rate of aeolian sand transport. Geomorphology 59, 53–62. https://doi.org/10.1016/j.geomorph.2003.09.005.
Sugiura, K., Nishimura, K., Maeno, N., Kimura, T., 1998. Measurements of snow mass flux and transport rate at different particle diameters in drifting snow. Cold Reg. Sci. Technol. 27, 83–89. https://doi.org/10.1016/S0165-232X(98)00002-0.
Sugiura, K., Maeno, N., 2000. Wind-tunnel measurements of restitution coefficients and ejection number of snow particles in drifting snow: determination of splash functions. Boundary-Layer Meteorol. 95, 123–143. https://doi.org/10.1023/A:1002681026929.
Syms, G.F., 2008. Simulation of simplified-frigate airwakes using a lattice-Boltzmann method. J. Wind Eng. Ind. Aerod. 96, 1197–1206. https://doi.org/10.1016/j.jweia.2007.06.040.
Tagliavini, G., McCorquodale, M., Westbrook, C., Corso, P., Krol, Q., Holzner, M., 2021. Drag coefficient prediction of complex-shaped snow particles falling in air beyond the Stokes regime. Int. J. Multiphas. Flow 140, 103652. https://doi.org/10.1016/j.ijmultiphaseflow.2021.103652.
Takeuchi, M., Ishimoto, K., Nohara, T., 1975. A study of drift snow transport. J. Jpn. Soc. Snow Ice 37, 114–121. https://doi.org/10.5331/seppyo.37.114 (in Japanese with English summary).
Takeuchi, M., 1980. Vertical profile and horizontal increase of drift-snow transport. J. Glaciol. 26, 481–492. https://doi.org/10.3189/S0022143000010996.
Tanji, S., Inatsu, M., Okaze, T., 2021. Development of a snowdrift model with the lattice Boltzmann method. Prog. Earth Planet. Sci. 8, 57. https://doi.org/10.1186/s40645-021-00449-0.
Tominaga, Y., Mochida, A., 1999. CFD prediction of flowfield and snowdrift around a building complex in a snowy region. J. Wind Eng. Ind. Aerod. 81, 273–282. https://doi.org/10.1016/S0167-6105(99)00023-9.
Tominaga, Y., Mochida, A., Okaze, T., Sato, T., Nemoto, M., Motoyoshi, H., Nakai, S., Tsutsumi, T., Otsuki, M., Uematsu, T., Yoshino, H., 2011. Development of a system for predicting snow distribution in built-up environments: combining a mesoscale meteorological model and a CFD model. J. Wind Eng. Ind. Aerod. 99, 460–468. https://doi.org/10.1016/j.jweia.2010.12.004.
Tominaga, Y., 2018. Computational fluid dynamics simulation of snowdrift around buildings: past achievements and future perspectives. Cold Reg. Sci. Technol. 150, 2–14. https://doi.org/10.1016/j.coldregions.2017.05.004.
Uematsu, T., Nakata, T., Takeuchi, K., Arisawa, Y., Kaneda, Y., 1991. Three-dimensional numerical simulation of snowdrift. Cold Reg. Sci. Technol. 20, 65–73. https://doi.org/10.1016/0165-232X(91)90057-N.
Vionnet, V., Martin, E., Masson, V., Guyomarc'h, G., Naaim-Bouvet, F., Prokop, A., Durand, Y., Lac, C., 2014. Simulation of wind-induced snow transport and sublimation in alpine terrain using a fully coupled snowpack/atmosphere model. Cryosphere 8, 395–415. https://doi.org/10.5194/tc-8-395-2014.
Wallace, J.M., 2016. Quadrant analysis in turbulence research: history and evolution. Annu. Rev. Fluid Mech. 48, 131–158. https://doi.org/10.1146/annurev-fluid-122414-034550.
Wang, Z., Huang, N., Pähtz, T., 2019. The effect of turbulence on drifting snow sublimation. Geophys. Res. Lett. 46, 11568–11575. https://doi.org/10.1029/2019GL083636.
Wang, Z., Jia, S., 2018. A simulation of a large-scale drifting snowstorm in the turbulent boundary layer. Cryosphere 12, 3841–3851. https://doi.org/10.5194/tc-12-3841-2018.
Watanabe, T., 2004. Large-eddy simulation of coherent turbulence structures associated with scalar ramps over plant canopies. Boundary-Layer Meteorol. 112, 307–341. https://doi.org/10.1023/B:BOUN.0000027912.84492.54.
Watanabe, T., 2009. LES study on the structure of coherent eddies inducing predominant perturbations in velocities in the roughness sublayer over plant canopies. J. Meteorol. Soc. Japan 87, 39–56. https://doi.org/10.2151/jmsj.87.39.
Watanabe, T., Shimoyama, K., Kawashima, M., Mizoguchi, Y., Inagaki, A., 2020. Large-eddy simulation of neutrally-stratified turbulent flow within and above plant canopy using the central-moments-based lattice Boltzmann method. Boundary-Layer Meteorol. 176, 35–60. https://doi.org/10.1007/s10546-020-00519-8.
Watanabe, T., Takagi, M., Shimoyama, K., Kawashima, M., Onodera, N., Inagaki, A., 2021. Coherent eddies transporting passive scalars through the plant canopy revealed by large-eddy simulations using the lattice Boltzmann method. Boundary-Layer Meteorol. 181, 39–71. https://doi.org/10.1007/s10546-021-00633-1.
Weil, J.C., Sullivan, P.P., Moeng, C.H., 2004. The use of large-eddy simulations in Lagrangian particle dispersion models. J. Atmos. Sci. 61, 2877–2887. https://doi.org/10.1175/JAS-3302.1.
White, F.M., 1974. Viscous Fluid Flow. McGraw-Hill, New York.
Xing, M., He, C., 2013. 3D ejection behavior of different sized particles in the grain-bed collision process. Geomorphology 187, 94–100. https://doi.org/10.1016/j.geomorph.2013.01.002.
Zhang, T., Zhou, X., 2023. Numerical simulations of snow saltation over flat terrain: development of snow transport. J. Wind Eng. Ind. Aerod. 204, 105472 https://doi.org/10.1016/j.jweia.2023.105472.
Zhou, X., Zhang, T., 2023. A review of computational fluid dynamics simulations of wind-induced snow drifting around obstacles. J. Wind Eng. Ind. Aerod. 234, 105350 https://doi.org/10.1016/j.jweia.2023.105350.
Zhou, X., Zhang, T., Liu, Z., Gu, M., 2023. An Eulerian-Lagrangian snow drifting model for gable roofs considering the effect of roof slope. J. Wind Eng. Ind. Aerod. 234, 105334 https://doi.org/10.1016/j.jweia.2023.105334.